An Extended Finite Element Method for Dislocations in Complex Geometries: Thin Films and Nanotubes ⋆

Jay Oswald, Robert Gracie, Roopam Khare, Ted Belytschko *,1

Department of Mechanical Engineering, Northwestern University, 2145 Sheridan Road, Evanston, IL 60208-3111, USA

Abstract

Dislocation models based on the Extended Finite Element Method (XFEM) are developed for thin shells such as carbon nanotubes (CNTs) and thin films. In shells, methods for edge dislocations, which move by glide, and prismatic dislocations, which move by climb, are described. In thin films, methods for dislocations with edge, screw and/or prismatic character are developed in three-dimensions. Singular enrichments are proposed which allow the Peach-Koehler force to be computed directly from the stress field along the dislocation line and give improved accuracy.

Key words: dislocations, extended finite element method, thin films, thin shells, carbon nanotubes

1 Introduction

Dislocation modeling has been performed predominantly by Green's functions methods and image field methods (1; 2; 3; 4; 5; 6). These methods are quite powerful in solving problems with relatively simple geometry; however, there is increasing interest in problems with more complex geometry, such as three-dimensional thin films, shells, such as nanotubes, and materials with inclusions. In such complex geometries, integral equation methods and image field

⋆ In honor of J. Tinsley Oden on his 70th birthday in recognition of his outstanding seminal contributions to computational mechanics.

* Corresponding author. Department of Mechanical Engineering, Northwestern University, 2145 Sheridan Road, Evanston, IL 60208-3111, USA. e-mail:tedbelytschko@northwestern.edu

[1] Walter P. Murphy and McCormick Professor of Mechanical Engineering

methods are generally inapplicable, since neither Green's functions nor the exact solutions for the image field for such geometries are usually available and are difficult to construct. In three-dimensional bodies, several methods have emerged to address the challenges of geometry and material interfaces: the discrete continuum method (7; 8), the superposition method of O'Day and Curtin (9), and the extended finite element method (10; 11).

In Gracie et al. (11), it was shown that accurate computations of the bulk strain energy of edge dislocations can be made with models consisting simply of a discontinuity on the glide plane with the extended finite element method (XFEM). This method employed no special treatment of the singular core. However, for such models the computation of the Peach-Koehler force involves the evaluation of a domain integral, which requires very fine mesh resolution in problems involving close range dislocation interactions and material interfaces. In (12) an alternative method for computing the Peach-Koehler force from an image stress was demonstrated in two dimensions using closed-form analytical solutions for dislocations in an infinite domain as an enrichment in the vicinity of the core.

This paper presents further developments in the modeling of dislocations by XFEM which was initiated in (11; 12; 10; 13) with emphasis on problems with complex geometry. These methods are based on the partition-of-unity concept proposed by Melenk and Babuška (14) and Duarte and Oden (15). In particular, the extension of the XFEM dislocation methods to three dimensions and cylindrical shells is described along with applications in thin films and nanotubes. To the best of our knowledge, this is the first finite element method for modeling dislocations in thin shells. As in (12), the Peach-Koehler force is computed without evaluating a domain integral. The enrichment is a transformation of two-dimensional closed form, infinite domain solutions for straight dislocations that approaches the correct solution as the distance to the core decreases to zero. To reduce the computational cost of evaluating this enrichment, a simple discontinuous step enrichment is applied on the glide plane away from the core.

We also describe the application of this method for modeling dislocations in single-walled carbon nanotubes (SWCNTs) and thin films. Our interest in dislocations in CNTs stems from some recent experiments at high temperatures (16; 17), where SWCNTs were observed to deformed plastically at 2000°C. Nardelli et al. (18) proposed a plastic failure mechanism for CNTs based on dislocation motion. It has been suggested that a Stone-Wales defect (19) can be seen as a pair of dislocations or as a dislocation dipole. Ding et al. (20) proposed a mechanism based on a two-atom vacancy defect that can also be viewed as a dislocation dipole, which can climb and glide. Mori et al. (21) and Zhang et al. (22) performed molecular mechanics (MM) simulations on small CNTs under bending and tensile loading, respectively, to obtain glide energet-

ics of 5-7 pairs. The computational expense of MM analysis is significant, so as the size of the nanotubes being studied increases, continuum-based analysis becomes an attractive alternative.

Modeling a CNT in a continuum-based analysis is not without precedent. Defect-free CNTs have successfully been modeled as thin shells (23; 24; 25; 26; 27; 28). It was shown in (26) that continuum models of pristine CNTs correctly capture large deformations and buckling instabilities. Therefore it is not unreasonable to expect that the methods proposed here will accurately model dislocation defects in nanotubes of any size.

Thin films are the second application area described here. In thin films with sub-micron dimensions, material interfaces interact strongly with dislocations to influence the strength of the films and give rise to size effects. Understanding the behavior of dislocations in thin films is critical for the improvement of the reliability of many micro-electro-mechanical systems (29). Dislocation models based on the superposition of infinite domain solutions (30; 3; 4; 5) have been used extensively to model dislocation threading in thin films (31; 32; 33). The models are usually based on the superposition of isotropic linear elastic solutions and idealized material interfaces and boundary conditions. Complex geometries are difficult to treat by these methods. The method described here can directly simulate arbitrary complex geometries as it is based on the finite element method. We will give some representative calculations to demonstrate the potential of the method.

The paper is organized as follows: in Section 2, methods for modeling dislocations in thin shells by the Extended Finite Element Method (XFEM) are described. Dislocations are modeled as two-dimensional features on a three-dimensional manifold. Dislocations created from a Stone-Wales defect are modeled as a pair of edge dislocations, while dislocations created by a two atom vacancy are modeled by a pair of prismatic dislocations. In Section 3, methods for simulating dislocations in thin films by XFEM are described, where dislocations will be modeled as planar surfaces of slip in a three-dimensional domain. Results of numerical examples are shown in Section 4, and in Section 5 we give our concluding remarks.

2 XFEM for dislocations in shells

In this section we summarize the Kirchhoff-Love theory for thin shells, describe the XFEM displacement approximations for modeling edge and prismatic dislocations in shells, and derive the discrete equilibrium equations.

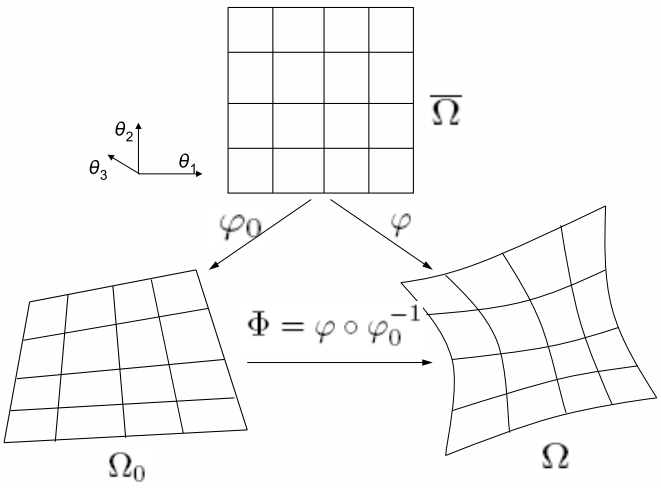

Fig. 1. Sketch of the reference domain Ω_0, current domain Ω, and parametric domain $\overline{\Omega}$ and the mappings between them.

2.1 Shell equations

Let the reference domain and the current domain of the body be denoted by Ω_0 and Ω, respectively, and let Γ_0 and Γ be their respective boundaries. Displacement $\overline{\mathbf{u}}$ is prescribed on Γ_{0u} and traction $\overline{\mathbf{t}}_0$ is prescribed on Γ_{0t}. Let Γ_{0d}^{λ} represent the interior discontinuities in the reference domain due to the dislocations, where $\lambda = 1 \dots n_{\mathrm{D}}$ and n_{D} is the total number of dislocations in the body. Let Γ_d^{λ} denote the same discontinuities in the current configuration. We also define a parametric body $\overline{\Omega}$ with boundary $\overline{\Gamma}$, as shown in Fig. 1.

We will start with a general nonlinear shell theory, but the development will subsequently be restricted to the linear case. The undeformed reference and deformed current configurations are mapped to the parametric body by differentiable and invertible maps φ_0 and φ, respectively, such that $\varphi_0(\overline{\Omega}) = \Omega_0$ and $\varphi(\overline{\Omega}) = \Omega$. The deformation map is then given as

$$\Phi = \varphi \circ \varphi_0^{-1}. \tag{1}$$

The position vectors $\mathbf{x}$ and $\mathbf{X}$ of a material point in the current and the reference domain, respectively, can be written in terms of the parametric coordinates $\{\theta_1, \theta_2, \theta_3\}$ such that

$$\mathbf{X}(\theta_1, \theta_2, \theta_3) = \mathbf{R}(\theta_1, \theta_2) + \theta_3 \mathbf{g}_3^0, \tag{2}$$

$$\mathbf{x}(\theta_1, \theta_2, \theta_3) = \mathbf{r}(\theta_1, \theta_2) + \theta_3 \mathbf{g}_3, \tag{3}$$

where the functions $\mathbf{R}(\theta_1, \theta_2)$ and $\mathbf{r}(\theta_1, \theta_2)$ are the parametric mappings of the shell in the reference and the deformed configuration, respectively. The corresponding convected bases of the tangents of the deformed body, $\mathbf{g}_\alpha$, and undeformed body, $\mathbf{g}^0_\alpha$, are given by

$$\mathbf{g}_\alpha = \varphi_{,\alpha},\ \mathbf{g}^0_\alpha = \varphi^0_{,\alpha},\quad \alpha = 1, 2. \tag{4}$$

The covariant components of the metric tensor of the surface of Ω and Ω_0 can be calculated by

$$g_{\alpha\beta} = \mathbf{g}_\alpha \cdot \mathbf{g}_\beta,\ g^0_{\alpha\beta} = \mathbf{g}^0_\alpha \cdot \mathbf{g}^0_\beta,\quad \beta = 1, 2, \tag{5}$$

and the contravariant components of the deformed surface metric tensor, $G_{\alpha\beta}$, and the undeformed surface metric tensor, $G^0_{\alpha\beta}$, are obtained by taking the inverse of the deformed and undeformed covariant metric tensors, respectively.

The displacement of the mid-surface $\mathbf{u}$ is given by

$$\mathbf{u}(\theta_1, \theta_2) = \mathbf{r}(\theta_1, \theta_2) - \mathbf{R}(\theta_1, \theta_2). \tag{6}$$

The membrane strain $\boldsymbol{\epsilon}^m$ and bending strain $\boldsymbol{\epsilon}^b$ are given by the following expressions (34):

$$\epsilon^m_{\alpha\beta}(\mathbf{u}) = \frac{1}{2}(\mathbf{g}^0_\alpha \cdot \mathbf{u}_{,\beta} + \mathbf{g}^0_\beta \cdot \mathbf{u}_{,\alpha}), \tag{7}$$

$$\begin{aligned}\epsilon^b_{\alpha\beta}(\mathbf{u}) = -\mathbf{g}^0_3 \cdot \mathbf{u}_{,\alpha\beta} + \frac{1}{|g^0|}[(\mathbf{g}^0_{\alpha,\beta} \times \mathbf{g}^0_2) \cdot \mathbf{u}_{,1} + (\mathbf{g}^0_1 \times \mathbf{g}^0_{\alpha,\beta}) \cdot \mathbf{u}_{,2}] \\ + \frac{(\mathbf{g}^0_{\alpha,\beta} \cdot \mathbf{g}^0_2)}{|g^0|}[(\mathbf{g}^0_2 \times \mathbf{g}^0_3) \cdot \mathbf{u}_{,1} + (\mathbf{g}^0_3 \times \mathbf{g}^0_1) \cdot \mathbf{u}_{,2}],\end{aligned} \tag{8}$$

where

$$\mathbf{g}^0_3 = \frac{\mathbf{g}^0_1 \times \mathbf{g}^0_2}{|\mathbf{g}^0_1 \times \mathbf{g}^0_2|} \tag{9}$$

and

$$|g^0| = |\mathbf{g}^0_1 \times \mathbf{g}^0_2|. \tag{10}$$

$\mathbf{g}^0_3$ coincides with the unit normal to the undeformed surface. In the similar manner, $\mathbf{g}_3$ and $|g|$ are calculated from the deformed surface.

The principal of virtual work for a thin shell under linear elastic assumptions (34; 35) is given as: find $\mathbf{u} \in \mathcal{U}$, such that

$$\int_\Omega \left[\eta^1 \delta\boldsymbol{\epsilon}^{m\mathrm{T}}(\mathbf{v})\mathbf{C}\boldsymbol{\epsilon}^m(\mathbf{u}) + \eta^2 \delta\boldsymbol{\epsilon}^{b\mathrm{T}}(\mathbf{v})\mathbf{C}\boldsymbol{\epsilon}^b(\mathbf{u})\right] \mathrm{d}\Omega - \int_\Omega \mathbf{q}\cdot\mathbf{v}\mathrm{d}\Omega - \int_{\Gamma_\mathrm{t}} \bar{\mathbf{t}}\cdot\mathbf{v}\mathrm{d}\Gamma, \forall \mathbf{v} \in \mathcal{U}_0, \tag{11}$$

where $\eta^1 = Eh/(1-\nu^2)$, $\eta^2 = Eh^3/12(1-\nu^2)$, h is the thickness of the shell, E is Young's modulus, ν is Poisson's ratio, $\mathbf{q}$ is the body force and $\bar{\mathbf{t}}$ is the traction applied on boundary Γ_{t} and $\mathbf{C}$ is given by

$$\mathbf{C} = \begin{bmatrix} (G^0_{11})^2 & \nu G^0_{11} G^0_{22} + (1-\nu)(G^0_{12})^2 & G^0_{11} G^0_{12} \\ & (G^0_{22})^2 & G^0_{22} G^0_{12} \\ \text{sym.} & & \frac{1}{2}[(1-\nu) G^0_{11} G^0_{22} + (1+\nu)(G^0_{12})^2] \end{bmatrix}. \tag{12}$$

Note that Eq. (8) involves the second derivative of the displacement and therefore C^1 continuity is required for the displacement field. The spaces $\mathcal{U}_0$ and $\mathcal{U}$ in Eq. (11) are defined as

$$\mathcal{U}_0 = \{\mathbf{u} \in H^2(\Omega \setminus \Gamma_d), \mathbf{u} = 0 \text{ on } \Gamma_u\}, \tag{13}$$

$$\mathcal{U} = \{\mathbf{u} \in H^2(\Omega \setminus \Gamma_d), \mathbf{u} = \overline{\mathbf{u}} \text{ on } \Gamma_u\}. \tag{14}$$

2.2 The tangential space and the exponential map

In the remainder of the development of the method for thin shells, we omit the superscript and subscript 0 and refer to both the material and reference coordinates as $\mathbf{x}$ since we no longer differentiate between coordinates or quantities in the reference and current configurations. In this section we define a map that transforms a vector tangent to the cylindrical surface to a vector that starts and ends on the cylinder surface, so that the dislocation enrichment can be transformed from the parametric domain to current domain.

We use the exponential map as in Arroyo and Belytschko (36). Let $T_{\mathbf{x}_A}\Omega$ be the tangent space to Ω centered at $\mathbf{x}_A$ with basis vectors $\mathbf{g}_1$ and $\mathbf{g}_2$ defined in (4). Let $\exp_{\mathbf{x}_A}\left(\mathbf{u}^\theta\right)$ be the exponential map which takes a vector $\mathbf{u}^\theta = u^\theta_1 \mathbf{g}_1 + u^\theta_2 \mathbf{g}_2$, in the tangent space $T_{\mathbf{x}_A}\Omega$ centered at $\mathbf{x}_A$, to a point $\mathbf{x}_B$ on Ω, such that the distance from $\mathbf{x}_A$ to $\mathbf{x}_B$ along Ω is $\|\mathbf{u}^\theta\|$. We denote by $\mathcal{F}_{\varphi(\boldsymbol{\theta})}$ the map which takes a vector $\mathbf{u}^\theta = u^\theta_1 \mathbf{g}_1 + u^\theta_2 \mathbf{g}_2$, in the tangent space $T_{\varphi(\boldsymbol{\theta})}\Omega$, centered at $\varphi(\boldsymbol{\theta})$, $\boldsymbol{\theta} \in \bar{\Omega}$, into a vector $\mathbf{u} = u_1 \mathbf{e}_1 + u_2 \mathbf{e}_2 + u_3 \mathbf{e}_3$. It is defined as

$$\mathbf{u}(\boldsymbol{\theta}) = \mathcal{F}_{\varphi(\boldsymbol{\theta})}\left(\mathbf{u}^\theta(\boldsymbol{\theta})\right) = \exp_{\varphi(\boldsymbol{\theta})}\left(\mathbf{u}^\theta(\boldsymbol{\theta})\right) - \varphi(\boldsymbol{\theta}), \boldsymbol{\theta} \in \bar{\Omega}. \tag{15}$$

For a cylindrical shell of radius R, where the global basis vector $\mathbf{e}_1 \equiv \mathbf{e}^\theta_1$ is the axis of the cylinder, the maps φ, $\exp_{\varphi(\boldsymbol{\theta})}$, and $\mathcal{F}_{\varphi(\boldsymbol{\theta})}$ have the following

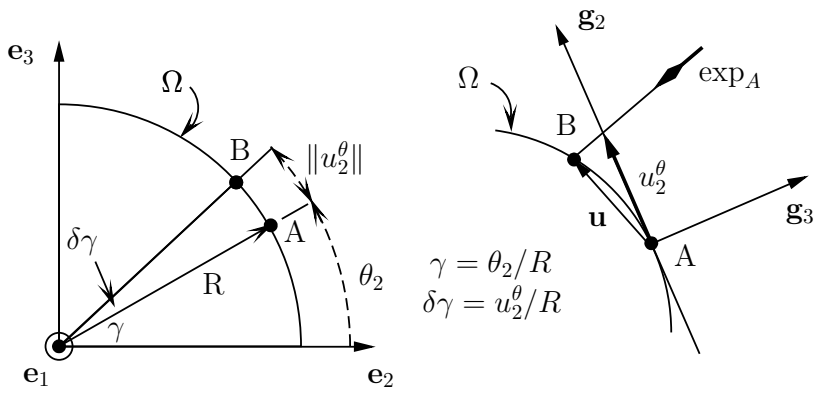

Fig. 2. Illustration of the definition of the exponential map $\exp_A$ and the map $\mathcal{F}_A$ for a cylindrical shell Ω of radius R. The exponential map takes the vector $\mathbf{u}^\theta$ onto the point B on Ω, while $\mathcal{F}_A$ maps the vector $\mathbf{u}^\theta$ to $\mathbf{u}$.

analytical forms:

$$\varphi\left(\theta_1,\theta_2\right) = \left\{\begin{array}{c} \theta_1 \\ R\cos\left(\theta_2/R\right) \\ R\sin\left(\theta_2/R\right) \end{array}\right\}, \tag{16}$$

$$\exp_{\varphi(\boldsymbol{\theta})}\left(\mathbf{u}^\theta\left(\theta_1,\theta_2\right)\right) = \left\{\begin{array}{c} u_1^\theta + \theta_1 \\ R\cos\left(\theta_2/R + u_2^\theta/R\right) \\ R\sin\left(\theta_2/R + u_2^\theta/R\right) \end{array}\right\}, \tag{17}$$

and

$$\mathcal{F}_{\varphi(\boldsymbol{\theta})}\left(\mathbf{u}^\theta\left(\theta_1,\theta_2\right)\right) = \left\{\begin{array}{c} u_1^\theta \\ R\left(\cos\left(\theta_2/R + u_2^\theta/R\right) - \cos\left(\theta_2/R\right)\right) \\ R\left(\sin\left(\theta_2/R + u_2^\theta/R\right) - \sin\left(\theta_2/R\right)\right) \end{array}\right\}. \tag{18}$$

The mappings in (17-18) are depicted in Fig. 2 for a cross-section of the cylinder perpendicular to $\mathbf{e}_1$.

2.3 Displacement approximations

In XFEM, the displacement approximation is decomposed into a standard continuous part $\mathbf{u}^{\mathrm{C}}$ and an enriched discontinuous part $\mathbf{u}^{\mathrm{D}}$, such that

$$\mathbf{u}(\theta_1, \theta_2) = \mathbf{u}^{\mathrm{C}}(\theta_1, \theta_2) + \mathbf{u}^{\mathrm{D}}(\theta_1, \theta_2), \tag{19}$$

where $\mathbf{u}^{\mathrm{C}}$ is given by the standard finite element approximation

$$\mathbf{u}^{\mathrm{C}}(\theta_1, \theta_2) = \sum_I N_I(\theta_1, \theta_2)\mathbf{u}_I, \tag{20}$$

where N_I are the finite element interpolants and $\mathbf{u}_I$ are the nodal degrees of freedom. Let $\mathbf{e}_1^0$, $\mathbf{e}_2^0$, $\mathbf{e}_3^0$ be the basis vectors of the reference coordinate system and $\mathbf{e}_1^\theta$, $\mathbf{e}_2^\theta$, $\mathbf{e}_3^\theta$ be the basis vectors of the parametric coordinate system.

The geometry of a dislocation pair is described in the parametric coordinate system by two level set functions $f(\theta_1, \theta_2)$ and $\mathrm{g}(\theta_1, \theta_2)$, such that the glide plane is given by $f(\theta_1, \theta_2) = 0$ and $\mathrm{g}(\theta_1, \theta_2) < 0$ and the dislocation cores are given by the points of intersection of the contours $f(\theta_1, \theta_2) = 0$ and $\mathrm{g}(\theta_1, \theta_2) = 0$, as shown in Fig. 3. In addition, we associate a scalar with each dislocation core: +1 or -1 when the sense of the dislocation line passing through the core is in the direction of $+\mathbf{e}_3^\theta$ and $-\mathbf{e}_3^\theta$, respectively. For every dislocation pair, there is always one dislocation with a positive sense and one with a negative sense.

We also define a local coordinate system at each of these cores. Let $\widehat{\mathbf{e}}_1^{\theta+}$, $\widehat{\mathbf{e}}_2^{\theta+}$ and $\widehat{\mathbf{e}}_1^{\theta-}$, $\widehat{\mathbf{e}}_2^{\theta-}$ be the basis vectors of the local coordinate system at the core with positive and negative sense, respectively, as shown in Fig. 3. These basis vectors are constructed from the level sets $f(\theta_1, \theta_2)$ and $\mathrm{g}(\theta_1, \theta_2)$:

$$\begin{aligned} \widehat{\mathbf{e}}_1^{\theta\diamond} &= \boldsymbol{\nabla}^\theta \mathrm{g}|_{\boldsymbol{\theta}_c^\diamond} \\ \widehat{\mathbf{e}}_2^{\theta\diamond} &= \boldsymbol{\nabla}^\theta f|_{\boldsymbol{\theta}_c^\diamond} \\ \diamond &\equiv +, - , \end{aligned} \tag{21}$$

where $\boldsymbol{\theta}_c^\diamond$ is the location of the positive or negative core in the parametric coordinate system and $\boldsymbol{\nabla}^\theta$ is the gradient operator with respect to the parametric coordinate system.

2.3.1 Edge dislocations

The enriched part of the displacement field for an edge dislocation dipole is given by

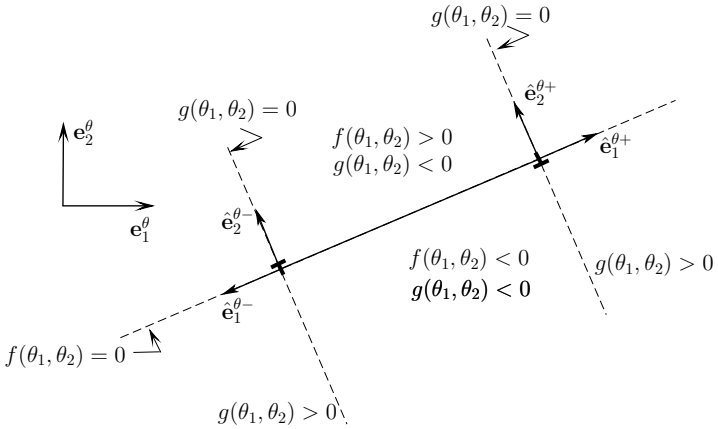

Fig. 3. Definition of a pair of edge dislocations in the parametric domain by level sets $f(\mathbf{x})$ and $g(\mathbf{x})$, and the definition of local core coordinate systems $(\hat{\mathbf{e}}_1^{\theta+}, \hat{\mathbf{e}}_2^{\theta+})$ and $(\hat{\mathbf{e}}_1^{\theta-}, \hat{\mathbf{e}}_2^{\theta-})$.

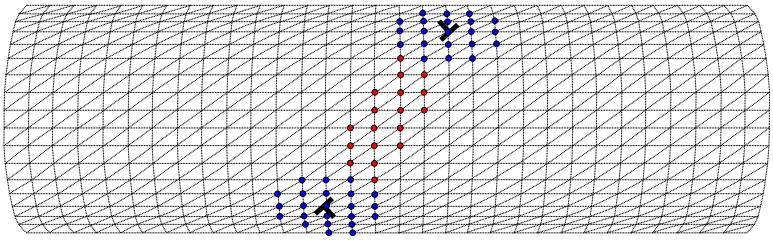

Fig. 4. An XFEM model of an edge dislocation pair in a CNT. The bigger and darker nodes belong to $\mathrm{S}^{\infty,\diamond}$ and the smaller and lighter nodes belong to S^{H}.

$$\begin{aligned}\mathbf{u}^{\mathrm{D}}(\theta_1,\theta_2) = &\textstyle\sum_{J\in \mathrm{S}^H} N_J(\theta_1,\theta_2)[\boldsymbol{\Psi}^H(\theta_1,\theta_2) - \boldsymbol{\Psi}_J^H] \\ &+ \textstyle\sum_{K\in \mathrm{S}^{\infty,+}} N_K(\theta_1,\theta_2)[\boldsymbol{\Psi}^{\infty,+}(\theta_1,\theta_2) - \boldsymbol{\Psi}_K^{\infty,+}] \\ &+ \textstyle\sum_{L\in \mathrm{S}^{\infty,-}} N_L(\theta_1,\theta_2)[\boldsymbol{\Psi}^{\infty,-}(\theta_1,\theta_2) - \boldsymbol{\Psi}_L^{\infty,-}]\,,\end{aligned} \tag{22}$$

where $\boldsymbol{\Psi}_J^H = \boldsymbol{\Psi}_J^H(\theta_1^J,\theta_2^J)$, $\boldsymbol{\Psi}_K^{\infty,+} = \boldsymbol{\Psi}_K^{\infty,+}(\theta_1^K,\theta_2^K)$ and $\boldsymbol{\Psi}_L^{\infty,-} = \boldsymbol{\Psi}_L^{\infty,-}(\theta_1^L,\theta_2^L)$. θ_1^J and θ_2^J are the parametric coordinates of node J. A node K is in $\mathrm{S}^{\infty,+}$ if $||\boldsymbol{\theta}_K - \boldsymbol{\theta}_c^+|| < \rho^+$, is in $\mathrm{S}^{\infty,-}$ if $||\boldsymbol{\theta}_K - \boldsymbol{\theta}_c^-|| < \rho^-$ or is in S^H if node K is not in $\mathrm{S}^{\infty,+}$ nor $\mathrm{S}^{\infty,-}$ and the support of node K is cut by $f(\theta_1,\theta_2)=0$. Fig. 4 shows the nodes in the sets $\mathrm{S}^{\infty,+}$, $\mathrm{S}^{\infty,-}$ and S^{H} for a mesh of a CNT with a dislocation pair.

The enrichment vector fields at $\varphi(\boldsymbol{\theta})$ are first defined in the tangent space and are then mapped by $\mathcal{F}_{\varphi(\boldsymbol{\theta})}$ to displacements in the global coordinate system. For example,

$$\boldsymbol{\Psi}^H(\theta_1,\theta_2) = \mathcal{F}_{\varphi(\boldsymbol{\theta})}\left(\boldsymbol{\Psi}_\theta^H(\theta_1,\theta_2)\right)\,, \tag{23}$$

where

$$\boldsymbol{\Psi}_\theta^H(\theta_1,\theta_2) = \mathbf{b}_\theta H(-f(\theta_1,\theta_2)g(\theta_1,\theta_2))\,, \tag{24}$$

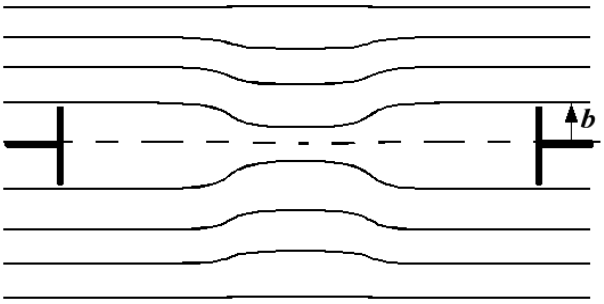

Fig. 5. Prismatic dislocation in a two-dimensional sheet.

$H(\cdot)$ is the Heaviside step function and $\mathbf{b}_\theta$ is the image of the Burgers vector $\mathbf{b}$ in the parametric domain. This means that the dislocation is defined by a constant slip across the glide plane in the parametric domain. Its image in the shell will vary with the location of the discontinuity.

The singular core enrichment $\mathbf{\Psi}^{\infty,\diamond}(\theta_1,\theta_2)$ is defined in a similar way, so

$$\mathbf{\Psi}^{\infty,\diamond}(\theta_1,\theta_2) = \mathcal{F}_{\varphi(\boldsymbol{\theta})}\left(\mathbf{\Psi}_\theta^{\infty,\diamond}(\theta_1,\theta_2)\right), \diamond = +,- \,, \tag{25}$$

where

$$\mathbf{\Psi}_\theta^{\infty,\diamond}(\theta_1,\theta_2) = \mathbf{T}^\diamond \cdot \mathbf{u}^{\infty,\diamond}(\theta_1^\diamond,\theta_2^\diamond), \diamond = +,- \,, \tag{26}$$

The point $(\theta_1^\diamond,\theta_2^\diamond)$ is defined with respect to the local core coordinate system $(\hat{\mathbf{e}}_1^{\theta\diamond},\hat{\mathbf{e}}_2^{\theta\diamond})$ in the parametric domain and $\mathbf{T}^\diamond$ is the rotation matrix between the local parametric coordinate system $(\hat{\mathbf{e}}_1^{\theta\diamond},\hat{\mathbf{e}}_2^{\theta\diamond})$ and the global parametric coordinate system $(\mathbf{e}_1^\theta,\mathbf{e}_2^\theta)$. So, the rotation matrix in (26) is

$$\mathbf{T}^\diamond = \begin{bmatrix} \mathbf{e}_1^\theta \cdot \widehat{\mathbf{e}}_1^{\theta\diamond} & \mathbf{e}_1^\theta \cdot \widehat{\mathbf{e}}_2^{\theta\diamond} \\ \mathbf{e}_2^\theta \cdot \widehat{\mathbf{e}}_1^{\theta\diamond} & \mathbf{e}_2^\theta \cdot \widehat{\mathbf{e}}_2^{\theta\diamond} \end{bmatrix}, \diamond = +,- \,. \tag{27}$$

and $\mathbf{u}^{\infty,\diamond}(\theta_1^\diamond,\theta_2^\diamond)$ is the plane stress solution for an edge dislocation in an infinite domain given by

$$\mathbf{u}^{\infty,\diamond}(\theta_1^\diamond,\theta_2^\diamond) = b_\theta \frac{1}{2\pi}\begin{bmatrix} \left(\tan^{-1}\left(\frac{\theta_2^\diamond}{\theta_1^\diamond}\right) + \frac{\theta_1^\diamond\theta_2^\diamond}{2(1-\nu)(\theta_1^{\diamond 2}+\theta_2^{\diamond 2})}\right) \\ -\left(\frac{1-2\nu}{4(1-\nu)}\ln(\theta_1^{\diamond 2}+\theta_2^{\diamond 2}) + \frac{\theta_1^{\diamond 2}-\theta_2^{\diamond 2}}{4(1-\nu)(\theta_1^{\diamond 2}+\theta_2^{\diamond 2})}\right) \end{bmatrix}. \tag{28}$$

where b_θ is the magnitude of the Burgers vector in the parametric domain.

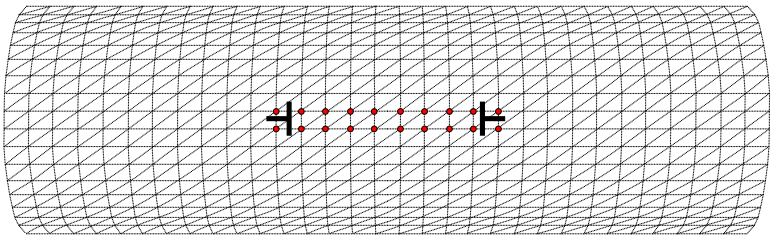

Fig. 6. An XFEM model of a prismatic dislocation pair in a CNT with nodes in $\mathrm{S^P}$ indicated. For clarity only the top surface is shown.

We note here that both the magnitude and direction of $\mathbf{b}_\theta$ are constant in the parametric domain, but in the reference domain, $\mathbf{b}$ depends on the location and orientation of the dislocation and the curvature of the shell.

2.3.2 Prismatic dislocations

A prismatic dislocation dipole can be created by either removing a row of atoms from the lattice or inserting an extra row of atoms, as shown in Fig. 5. We have used a step enrichment function to model this type of dislocation as proposed in (11). The discontinuous part of the displacement approximation for a prismatic dislocation is

$$\mathbf{u}^{\mathrm{D}}(\theta_1,\theta_2) = \sum_{J\in \mathrm{S}^P} N_J(\theta_1,\theta_2)[\mathbf{\Psi}^P(\theta_1,\theta_2) - \mathbf{\Psi}^P_J], \tag{29}$$

where $\mathbf{\Psi}^P_J = \mathbf{\Psi}^P_J(\theta^J_1,\theta^J_2)$. The nodal set S^{P} is the set of all the nodes of the elements cut by $f(\theta_1,\theta_2) = 0$ and $\mathrm{g}(\theta_1,\theta_2) < 0$. Fig. 6 shows the enriched nodes of a CNT containing a prismatic dislocation pair. Following the same procedure as with the edge dislocation enrichment, $\mathbf{\Psi}^P(\theta_1,\theta_2)$ is defined in terms of a two-dimensional field $\mathbf{\Psi}^P_\theta(\theta_1,\theta_2)$ defined as:

$$\mathbf{\Psi}^P_\theta(\theta_1,\theta_2) = \mathbf{b}_\theta H(-f(\theta_1,\theta_2)g(\theta_1,\theta_2)). \tag{30}$$

where $\mathbf{b}_\theta$ is perpendicular to $f(\theta_1,\theta_2) = 0$.

2.4 Discrete equations

Substituting Eqs. (20) and either (22) or (29) into Eq. (19) and Eq. (19) into Eq. (11) yields the following discrete equations

$$\mathbf{Kd} = \mathbf{f}^{\mathrm{ext}} + \mathbf{f}^{\mathrm{d}}, \tag{31}$$

where

$$\mathbf{f}_I^{\text{ext}} = \int_\Omega \mathbf{N}_I^{\mathrm{T}} \mathbf{q} \mathrm{d}\Omega + \int_{\Gamma_{\mathrm{t}}} \mathbf{N}_{\mathrm{I}}^{\mathrm{T}} \bar{\mathbf{t}} \mathrm{d}\Gamma, \tag{32}$$

and where $\mathbf{d}$ is a vector of nodal unknowns. The stiffness matrix $\mathbf{K}$ is given by

$$\mathbf{K}_{IJ} = \int_\Omega \left[\eta^1 (\mathbf{M}^I)^{\mathrm{T}} \mathbf{C} \mathbf{M}^J + \eta^2 (\mathbf{B}^I)^{\mathrm{T}} \mathbf{C} \mathbf{B}^J \right] \mathrm{d}\Omega \,, \tag{33}$$

where

$$\mathbf{M}^I = \begin{bmatrix} N_{I,1}\mathbf{g}_1^0 \cdot \mathbf{e}_1 & N_{I,1}\mathbf{g}_1^0 \cdot \mathbf{e}_2 & N_{I,1}\mathbf{g}_1^0 \cdot \mathbf{e}_3 \\ N_{I,2}\mathbf{g}_1^0 \cdot \mathbf{e}_1 & N_{I,2}\mathbf{g}_1^0 \cdot \mathbf{e}_2 & N_{I,2}\mathbf{g}_1^0 \cdot \mathbf{e}_3 \\ (N_{I,2}\mathbf{g}_1^0 + N_{I,1}\mathbf{g}_2^0) \cdot \mathbf{e}_1 & (N_{I,2}\mathbf{g}_1^0 + N_{I,1}\mathbf{g}_2^0) \cdot \mathbf{e}_2 & (N_{I,2}\mathbf{g}_1^0 + N_{I,1}\mathbf{g}_2^0) \cdot \mathbf{e}_3 \end{bmatrix}, \tag{34}$$

$$\begin{Bmatrix} B_{1j}^I \\ B_{2j}^I \\ B_{3j}^I \end{Bmatrix} = \begin{bmatrix} \Big(-N_{I,11}\mathbf{g}_3^0 + \frac{1}{|g^0|}[N_{I,1}\mathbf{g}_{1,1}^0 \times \mathbf{g}_2^0 + N_{I,2}\mathbf{g}_1^0 \times \mathbf{g}_{1,1}^0 + \\ \quad \mathbf{g}_3^0 \cdot \mathbf{g}_{1,1}^0 (N_{I,1}\mathbf{g}_2^0 \times \mathbf{g}_3^0 + N_{I,2}\mathbf{g}_3^0 \times \mathbf{g}_1)]\Big) \cdot \mathbf{e}_j \\ \Big(-N_{I,22}\mathbf{g}_3^0 + \frac{1}{|g^0|}[N_{I,1}\mathbf{g}_{2,2}^0 \times \mathbf{g}_2^0 + N_{I,2}\mathbf{g}_1^0 \times \mathbf{g}_{2,2}^0 + \\ \quad \mathbf{g}_3^0 \cdot \mathbf{g}_{2,2}^0 (N_{I,1}\mathbf{g}_2^0 \times \mathbf{g}_3^0 + N_{I,2}\mathbf{g}_3^0 \times \mathbf{g}_1^0)]\Big) \cdot \mathbf{e}_j \\ \Big(-N_{I,12}\mathbf{g}_3^0 + \frac{1}{|g^0|}[N_{I,1}\mathbf{g}_{1,2}^0 \times \mathbf{g}_2^0 + N_{I,2}\mathbf{g}_1^0 \times \mathbf{g}_{1,2}^0 + \\ \quad \mathbf{g}_3^0 \cdot \mathbf{g}_{1,2}^0 (N_{I,1}\mathbf{g}_2^0 \times \mathbf{g}_3^0 + N_{I,2}\mathbf{g}_3^0 \times \mathbf{g}_1^0)]\Big) \cdot \mathbf{e}_j \end{bmatrix}, \tag{35}$$

and where $j = 1$ to 3 and $\mathbf{e}_1$, $\mathbf{e}_2$ and $\mathbf{e}_3$ are the global basis vectors.

The forces due to the dislocation $\mathbf{f}^d$ are given by

$$\mathbf{f}_I^{\mathrm{d}} = -\sum_{\lambda=1}^{n_D} \int_\Omega \left[\eta^1 (\mathbf{M}^I)^{\mathrm{T}} \mathbf{C} \boldsymbol{\epsilon}^m(\mathbf{u}^{D\lambda}) + \eta^2 (\mathbf{B}^I)^{\mathrm{T}} \mathbf{C} \boldsymbol{\epsilon}^b(\mathbf{u}^{D\lambda}) \right] \mathrm{d}\Omega \,, \tag{36}$$

where $\mathbf{u}^{D\lambda}$ is the discontinuous part of the displacement approximation for dislocation pair λ given by (22) or (29), $\boldsymbol{\epsilon}^m$ is the membrane strain (7), and $\boldsymbol{\epsilon}^b$ is the bending strain (8).

Note that $\mathbf{K}$ is the standard finite element stiffness matrix, which remains unaltered by the enrichment. The effects of the dislocations appear only through the external nodal forces. This is a major advantage for dislocation dynamics problems (which we have not treated here), since solving the above system for moving dislocations only requires one triangulation of the stiffness matrix when a direct solver is used. For further details on this method see (11; 12; 13).

While the above is limited to a linear elastic formulation, nonlinear materials can be formulated in a similar manner (13).

3 Dislocations in three-dimensional thin films

In this section we develop the discrete equations for modeling dislocations in thin films in three dimensions. We begin by introducing the weak form, followed by the definitions of dislocations by level sets. Next we discuss the enrichment of the standard finite element approximation and finally we give the discrete equations.

3.1 Weak Form

Consider a domain Ω with boundary Γ. The boundary Γ is decomposed into two parts Γ_t and Γ_u. On Γ_t tractions $\bar{\mathbf{t}}$ are applied and on Γ_u displacements $\bar{\mathbf{u}}$ are prescribed. The domain contains dislocations which are the result of slip across planar surfaces Ω_D^α, where $\alpha = 1$ to n_D and n_D is the number of such surfaces. We will refer to the surfaces Ω_D^α as slip surfaces. The boundaries Γ_D^α of the Ω_D^α are the dislocations lines. We denote the union of all slip surfaces by $\Omega_D = \cup_\alpha \Omega_D^\alpha$ and the union of all slip surface boundaries by $\Gamma_D = \cup_\alpha \Gamma_D^\alpha$. The equilibrium equations are obtained from the principle of virtual work for a linear elastic body in the absence of body forces: Find $\mathbf{u} \in \mathcal{V}$ such that

$$\int_\Omega \delta\boldsymbol{\epsilon}^\top (\mathbf{v})\, \mathbf{D}\, \boldsymbol{\epsilon}(\mathbf{u})\, d\Omega = \int_{\Gamma_t} \bar{\mathbf{t}} \cdot \mathbf{v}\, d\Gamma\,, \quad \forall \mathbf{v} \in \mathcal{V}_0\,, \tag{37}$$

where $\boldsymbol{\epsilon}$ is the strain in Voigt form and $\mathbf{D}$ is the Hookean tensor such that the Cauchy stress in Voigt form is given by $\boldsymbol{\sigma} = \mathbf{D}\,\boldsymbol{\epsilon}$. The spaces $\mathcal{V}$ and $\mathcal{V}_0$ are

$$\mathcal{V} = \{\mathbf{u} \mid \mathbf{u} \in H^1(\Omega \backslash \Gamma_D)\,,\ \mathbf{u} = 0 \text{ on } \Gamma_u\} \tag{38}$$

and

$$\mathcal{V}_0 = \{\mathbf{u} \mid \mathbf{u} \in H^1(\Omega \backslash \Gamma_D)\,,\ \mathbf{u} = \bar{\mathbf{u}} \text{ on } \Gamma_u\}\,. \tag{39}$$

3.2 Description of dislocations by level sets

As in the thin shell, we describe each slip surface α by two level sets $f^\alpha(\mathbf{x})$ and $g^\alpha(\mathbf{x})$, such that slip surface Ω_D^α is defined as $\Omega_D^\alpha = \{\mathbf{x} | f^\alpha(\mathbf{x}) = 0 \cap g^\alpha(\mathbf{x}) < 0\}$

and the corresponding dislocation line Γ_D^α is defined as $\Gamma_D^\alpha = \{\mathbf{x} | f^\alpha(\mathbf{x}) = 0 \cap g^\alpha(\mathbf{x}) = 0\}$. In addition, we require that $\boldsymbol{\nabla} f^\alpha(\mathbf{x})$ be perpendicular to $\boldsymbol{\nabla} g^\alpha(\mathbf{x})$. The sense or tangent of the dislocation curve α is given by $\boldsymbol{\xi}^\alpha(\mathbf{x}) = \boldsymbol{\nabla} g^\alpha(\mathbf{x}) \times \boldsymbol{\nabla} f^\alpha(\mathbf{x})$. The level sets $f(\mathbf{x})$ and $g(\mathbf{x})$ are shown in Fig. 7 for a single circular dislocation loop. The slip surface Ω_D is the circular area in the slip plane bounded by the dislocation loop, Γ_D, and with normal $\mathbf{n}$.

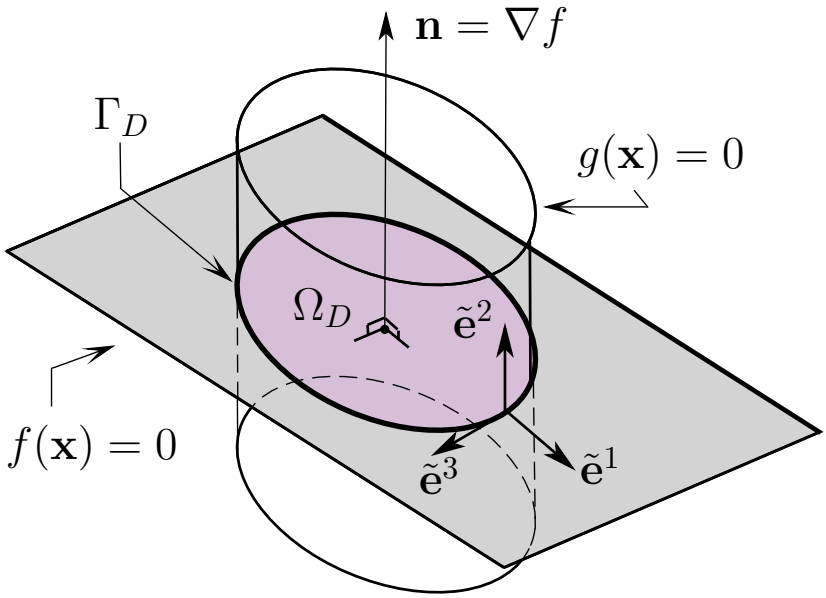

Fig. 7. Level set description of a single dislocation loop. The glide plane is defined by the $f(\mathbf{x}) = 0$ and the intersection of $g(\mathbf{x}) = 0$ and $f(\mathbf{x}) = 0$ defines the dislocation line Γ_D.

Because of the packing arrangements of various crystal lattices, each crystal has a finite number of energetically favorable slip systems. To simplify the tracking of the level set functions, we limit the slip surfaces to be planar, with normal directions corresponding to the close packed planes. Therefore, $\boldsymbol{\nabla} f^\alpha(\mathbf{x}) = \mathbf{n}^\alpha$, where $\mathbf{n}^\alpha$ is the normal to slip plane α. The number of possible planes with a given normal direction is constrained by the domain size and the lattice dimension, so all possible dislocation structures can be tracked on families of planes that correspond to the different slip systems in the crystal structure.

Since $\boldsymbol{\nabla} g^\alpha(\mathbf{x})$ is perpendicular to $\boldsymbol{\nabla} f^\alpha(\mathbf{x})$, $g^\alpha(\mathbf{x})$ need only be known on the plane $f^\alpha(\mathbf{x}) = 0$, and the value of $g^\alpha(\mathbf{x})$ for any point not on the glide plane is then determined by a projection. Therefore, a two-dimensional level set implementation is used for $g^\alpha(\mathbf{x})$.

To simplify the following discussion, we will limit ourselves to a domain with

a single dislocation and omit the superscript α. Let the plane $f(\mathbf{x}) = 0$ be denoted by Π and the normal of Π be denoted by $\mathbf{n}$. We define a local coordinate system $(\hat{\mathbf{e}}^1, \hat{\mathbf{e}}^2)$ on the plane, centered at the point $\mathbf{x}^Q$ in the global coordinate system. The level set $f(\mathbf{x})$ is given by

$$f(\mathbf{x}) = \left(\mathbf{x} - \mathbf{x}^Q\right) \cdot \mathbf{n} \,. \tag{40}$$

Let $\phi(\hat{\mathbf{x}})$ be the two-dimensional projection of $g(\mathbf{x})$ on Π and $\hat{\mathbf{x}}'$ be the local coordinates of the projection of $\mathbf{x}$ onto Π. We interpolate $g(\mathbf{x})$ and $\boldsymbol{\nabla} g(\mathbf{x})$ with the finite element shape functions $N_I(\mathbf{x})$, so

$$g(\mathbf{x}) = \sum_I N_I(\mathbf{x}) \phi_I \tag{41}$$

$$\boldsymbol{\nabla} g(\mathbf{x}) = \sum_I N_I(\mathbf{x}) \boldsymbol{\nabla} \phi_I = g_{,i}\, \mathbf{e}_i^0 \,, \tag{42}$$

where $\phi_I = \phi(\hat{\mathbf{x}}'_I)$, $\boldsymbol{\nabla}\phi_I = \boldsymbol{\nabla}\phi(\hat{\mathbf{x}}'_I)$, $\mathbf{x}_I$ are the global coordinates of node I and $\mathbf{e}_i^0$ are the basis vectors of the global coordinate system. Since $\boldsymbol{\nabla} g(\mathbf{x})$ is interpolated, generally $\|\boldsymbol{\nabla} g(\mathbf{x})\| \neq 1$. Therefore we define $\hat{g}(\mathbf{x})$ as the scalar function such that

$$\boldsymbol{\nabla} \hat{g}(\mathbf{x}) = \frac{\nabla g}{\|\nabla g\|} = \hat{g}_{,i}\, \mathbf{e}_i^0 \,. \tag{43}$$

3.3 Construction of a local dislocation coordinate system

For convenience, a local curvilinear coordinate system is constructed from the gradients of the level set functions $g(\mathbf{x})$ and $f(\mathbf{x})$. The basis vectors of the curvilinear coordinate system are

$$\begin{aligned} \tilde{\boldsymbol{e}}^{\mathbf{1}} &= \boldsymbol{\nabla} \hat{g} \\ \tilde{\boldsymbol{e}}^{\mathbf{2}} &= \boldsymbol{\nabla} f \qquad . \\ \tilde{\boldsymbol{e}}^{\mathbf{3}} &= \tilde{\boldsymbol{e}}^{\mathbf{1}} \times \tilde{\boldsymbol{e}}^{\mathbf{2}} \end{aligned} \tag{44}$$

These basis vectors are illustrated in Fig. 7 for a circular dislocation loop. $\tilde{\boldsymbol{e}}^{\mathbf{1}}$ is the local normal to the dislocation line in the plane of the slip surface, $\tilde{\boldsymbol{e}}^{\mathbf{2}}$ is normal to the slip surface and $\tilde{\boldsymbol{e}}^{\mathbf{3}}$ is the local tangent to the dislocation line.

For later developments, the gradients of the three local basis vectors with respect to the global coordinate system are defined. These are given by

$$\begin{aligned} \tilde{e}^1_{i,j} &= \hat{g}_{,pj} \\ \tilde{e}^2_{i,j} &= 0 \\ \tilde{e}^3_{i,j} &= \epsilon_{ipq}\hat{g}_{,pj}f_{,q} \end{aligned} \quad , \tag{45}$$

where

$$\hat{g}_{,ij} = \left(g_{,k}g_{,k}g_{,ij} - g_{,i}g_{,jk}g_{,k}\right)\left(g_{,k}g_{,k}\right)^{-3/2} \tag{46}$$

3.4 Displacement approximations

The core enrichment strategy is based on using a two-dimensional solution for a dislocation in the plane normal to the tangent of the dislocation line to model the near core behavior. This is combined with a tangential step function enrichment away from the core. A similar strategy was used for crack modeling in (37). We will refer to approximations that combine singular core and step function enrichments as the core enrichment or as the core enriched approximation. We call the approximation with no core enrichment the step enrichment.

The displacement field is again decomposed into a continuous part $\mathbf{u}^C(\mathbf{x})$ and a discontinuous part $\mathbf{u}^D(\mathbf{x})$, where

$$\mathbf{u}^C(\mathbf{x}) = \sum_I N_I(\mathbf{x})\,\mathbf{u}_I \tag{47}$$

and

$$\mathbf{u}^D(\mathbf{x}) = \sum_\alpha^{n_D} \sum_{J \in \mathcal{S}^\alpha} N_J(\mathbf{x})\left(\mathbf{\Psi}^\alpha(\mathbf{x}, \mathbf{b}^\alpha) - \mathbf{\Psi}^\alpha_J\right), \tag{48}$$

where $N_I(\mathbf{x})$ are the shape functions, $\mathbf{u}_I$ are the standard degrees of freedom of node I, $\mathcal{S}^\alpha$ is the set of enriched nodes for slip surface Ω^α_D, $\mathbf{b}^\alpha$ is the Burgers vector of dislocation α, $\mathbf{\Psi}^\alpha(\mathbf{x}, \mathbf{b}^\alpha)$ is the enrichment vector field for the dislocation due to slip surface Ω^α_D and $\mathbf{\Psi}^\alpha_I = \mathbf{\Psi}^\alpha(\mathbf{x}_I, \mathbf{b}^\alpha)$. In this form, the displacement at each node has been shifted; the nodal degrees of freedom $\mathbf{u}_I$ are the nodal displacements.

For each slip surface Ω^α_D, two enrichment subdomains are defined. The first subdomain contains the dislocation line, Γ^α_D, where the stress and strain fields are singular. It is denoted by Ω^α_S and is defined as the union of all elements such that the shortest distance from each node in the element to the dislocation line Γ^α_D is less than the enrichment radius. The second subdomain, Ω^α_H, is the union of all elements not contained in Ω^α_S, but that are cut by Ω^α_D. The set of enriched nodes $\mathcal{S}^\alpha$ is therefore defined as the nodes of all elements in $\Omega^\alpha_S \cup \Omega^\alpha_H$. Figure 8 illustrates the definition of the subdomains Ω^α_S and Ω^α_H for

a two-dimensional cross-section of a dislocation loop. We note that the displacement field does not satisfy compatibility on the boundary of Ω_S^α; however, since the enrichment always vanishes at the nodes due to the shifting of the approximation, compatibility is ensured at the nodes, and the gap between the elements at the border of Ω_S^α will decrease as element size is reduced.

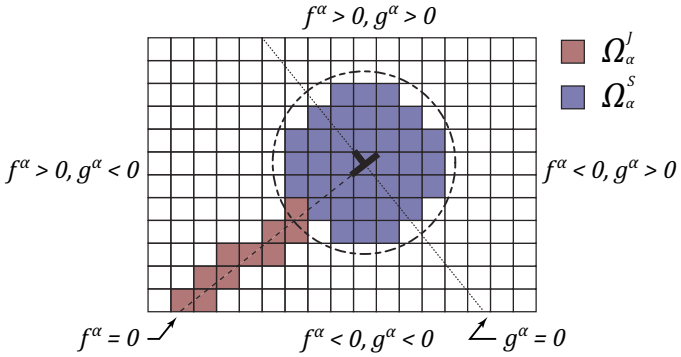

Fig. 8. Illustration of element-wise enrichment subdomains, Ω_S^α and Ω_H^α and the level sets $f^\alpha(\mathbf{x})$ and $g^\alpha(\mathbf{x})$ for a cross-section of a dislocation loop.

3.4.1 Enrichment function

The enrichment vector field, $\mathbf{\Psi}^\alpha(\mathbf{x}, \mathbf{b}^\alpha)$, for dislocation α is expressed as a function of the level set fields, $f^\alpha(\mathbf{x})$ and $g^\alpha(\mathbf{x})$ and of Burgers vector $\mathbf{b}^\alpha$. The enrichment is

$$\mathbf{\Psi}^\alpha(\mathbf{x}, \mathbf{b}^\alpha) = \begin{cases} \mathbf{R}\left(f^\alpha(\mathbf{x}), g^\alpha(\mathbf{x})\right) \cdot \tilde{\mathbf{\Psi}}\left(f^\alpha(\mathbf{x}), g^\alpha(\mathbf{x}), \mathbf{b}^\alpha\right) & \text{, for } \mathbf{x} \in \Omega_S^\alpha \\ H\left(f^\alpha(\mathbf{x})\right)\mathbf{b}^\alpha & \text{, for } \mathbf{x} \in \Omega_H^\alpha \\ 0 & \text{, otherwise} \end{cases}, \tag{49}$$

where H is the Heaviside step function. The rotation matrix is

$$\boldsymbol{R}\left(f^\alpha(\mathbf{x}), g^\alpha(\mathbf{x})\right) = \begin{bmatrix} \tilde{e}_1^1 & \tilde{e}_1^2 & \tilde{e}_1^3 \\ \tilde{e}_2^1 & \tilde{e}_2^2 & \tilde{e}_2^3 \\ \tilde{e}_3^1 & \tilde{e}_3^2 & \tilde{e}_3^3 \end{bmatrix} = \begin{bmatrix} \hat{g}_{,1}^\alpha & f_{,1}^\alpha & \hat{g}_{,2}^\alpha f_{,3}^\alpha - \hat{g}_{,3}^\alpha f_{,2} \\ \hat{g}_{,2}^\alpha & f_{,2}^\alpha & \hat{g}_{,3}^\alpha f_{,1}^\alpha - \hat{g}_{,1}^\alpha f_{,3}^\alpha \\ \hat{g}_{,3}^\alpha & f_{,3}^\alpha & \hat{g}_{,1}^\alpha f_{,2}^\alpha - \hat{g}_{,2}^\alpha f_{,1}^\alpha \end{bmatrix} \tag{50}$$

and $\tilde{\mathbf{\Psi}}(f^\alpha, g^\alpha, \mathbf{b}^\alpha)$ is the fine-scale enrichment field (or the core enrichment) in the local coordinate system.

The fine-scale enrichment field can be obtained either from analytical solutions or numerical computations (e.g. closed-form solutions for infinite straight dislocations, or refined finite element computations on a subdomain near the dislocation core.) The fine scale enrichments used here are based on two-dimensional infinite domain solution for straight dislocations in an isotropic material. The singular dislocation core enrichment function is

$$\tilde{\mathbf{\Psi}}\left(f,g,\mathbf{b}\right)=b_{\tilde{1}}\tilde{\mathbf{\Psi}}^{E}\left(f,g\right)+b_{\tilde{2}}\tilde{\mathbf{\Psi}}^{P}\left(f,g\right)+b_{\tilde{3}}\tilde{\mathbf{\Psi}}^{S}\left(f,g\right)\ , \tag{51}$$

where $b_{\tilde{k}}=R_{j\tilde{k}}b_j$ are the components of Burgers vector in the local coordinate system; $b_{\tilde{1}}$, $b_{\tilde{2}}$, and $b_{\tilde{3}}$ are the edge, prismatic and screw components of Burgers vector, respectively. The vector fields $\tilde{\mathbf{\Psi}}^{E}\left(f,g\right)$, $\tilde{\mathbf{\Psi}}^{P}\left(f,g\right)$, and $\tilde{\mathbf{\Psi}}^{S}\left(f,g\right)$ are the two-dimensional analytical displacement solutions for edge, prismatic and screw dislocations, respectively. They are given by

$$\begin{aligned}
\tilde{\mathbf{\Psi}}_{\tilde{1}}^{E}\left(f,g\right)&=\tfrac{1}{2\pi}\left[\tan^{-1}\left(\tfrac{f}{g}\right)+\tfrac{fg}{2(1-\nu)(f^2+g^2)}\right]\\
\tilde{\mathbf{\Psi}}_{\tilde{2}}^{E}\left(f,g\right)&=\tfrac{-1}{8\pi(1-\nu)}\left[(1-2\nu)\ln\left(f^2+g^2\right)+\tfrac{g^2-f^2}{f^2+g^2}\right]\\
\tilde{\mathbf{\Psi}}_{\tilde{3}}^{E}\left(f,g\right)&=0
\end{aligned}$$

$$\begin{aligned}
\tilde{\mathbf{\Psi}}_{\tilde{1}}^{P}\left(f,g\right)&=\tfrac{1}{8\pi(1-\nu)}\left[(1-2\nu)\ln\left(f^2+g^2\right)+\tfrac{f^2-g^2}{f^2+g^2}\right]\\
\tilde{\mathbf{\Psi}}_{\tilde{2}}^{P}\left(f,g\right)&=\tfrac{1}{2\pi}\left[\tan^{-1}\left(\tfrac{f}{g}\right)-\tfrac{fg}{2(1-\nu)(f^2+g^2)}\right]\\
\tilde{\mathbf{\Psi}}_{\tilde{3}}^{P}\left(f,g\right)&=0
\end{aligned} \tag{52}$$

$$\begin{aligned}
\tilde{\mathbf{\Psi}}_{\tilde{1}}^{S}\left(f,g\right)&=0\\
\tilde{\mathbf{\Psi}}_{\tilde{2}}^{S}\left(f,g\right)&=0\\
\tilde{\mathbf{\Psi}}_{\tilde{3}}^{S}\left(f,g\right)&=\tfrac{1}{2\pi}\tan^{-1}\left(\tfrac{f}{g}\right)
\end{aligned}$$

where ν is Poisson's ratio.

3.5 Discrete equations

The discrete equations are obtained by the substitution of (47), (48) into (37). The resulting system of equations is in the same form as that of the shell dislocation model and is given by

$$\mathbf{Kd}=\mathbf{f}^{\text{ext}}+\mathbf{f}^{\mathbf{\Psi}}\ , \tag{53}$$

where the nodal displacement are $\mathbf{d}$, the stiffness matrix is

$$\mathbf{K}_{IJ} = \int_{\Omega} \mathbf{B}_I^{\top} \mathbf{D} \mathbf{B}_J \, d\Omega \tag{54}$$

where $\mathbf{B}$ is the standard finite element B-matrix, such that the strain in Voigt form is $\boldsymbol{\epsilon} = \mathbf{B}\,\mathbf{d}$. The nodal forces due to the external forces are

$$\mathbf{f}_I^{\text{ext}} = \int_{\Gamma_t} \mathbf{N}_I^{\top} \bar{\mathbf{t}} \, d\Gamma \,, \tag{55}$$

where $\mathbf{N}_I = N_I \mathbf{I}$ and $\mathbf{I}$ is the identity matrix.

As was the case for the discrete shell equations, the stiffness matrix is the standard finite element stiffness matrix, and so does not depend on the number or the location of the dislocations. Therefore, it needs to only be assembled on the first time step of any dislocation dynamics simulation (we do not report any results of dislocation dynamics simulatons here).

The nodal forces due to the dislocations are

$$\mathbf{f}_I^{\boldsymbol{\Psi}} = \sum_{\alpha} \int_{\Omega} \mathbf{B}_I^{\top} \boldsymbol{\sigma}_D^{\alpha} \, d\Omega \,. \tag{56}$$

The enriched part of the stress due to dislocation α is

$$\boldsymbol{\sigma}_D^{\alpha} = \mathbf{D}\, \boldsymbol{\epsilon}_D^{\alpha} \,, \tag{57}$$

where $\boldsymbol{\epsilon}_D^{\alpha}$ is the corresponding enriched part of the strain. Stress and strain are decomposed as

$$\boldsymbol{\sigma}_D^{\alpha} = \bar{\boldsymbol{\sigma}}_D^{\alpha} + \hat{\boldsymbol{\sigma}}_D^{\alpha} \tag{58}$$

and

$$\boldsymbol{\epsilon}_D^{\alpha} = \bar{\boldsymbol{\epsilon}}_D^{\alpha} + \hat{\boldsymbol{\epsilon}}_D^{\alpha} \,, \tag{59}$$

where

$$\bar{\boldsymbol{\sigma}}_D^{\alpha} = \mathbf{D} \bar{\boldsymbol{\epsilon}}_D^{\alpha} \,, \tag{60}$$

$$\hat{\boldsymbol{\sigma}}_D^{\alpha} = \mathbf{D} \hat{\boldsymbol{\epsilon}}_D^{\alpha} \,, \tag{61}$$

$$\bar{\boldsymbol{\epsilon}}_D^{\alpha} = \sum_{J \in \mathcal{S}^{\alpha}} \mathbf{B}_J \boldsymbol{\Psi}_J^{\alpha} \tag{62}$$

and

$$\hat{\boldsymbol{\epsilon}}_D^{\alpha} = \begin{bmatrix} \boldsymbol{\Psi}_{1,1}^{\alpha} \\ \boldsymbol{\Psi}_{2,2}^{\alpha} \\ \boldsymbol{\Psi}_{1,2}^{\alpha} + \boldsymbol{\Psi}_{2,1}^{\alpha} \end{bmatrix} . \tag{63}$$

Using the definition (58), equation (56) is rewritten as

$$\mathbf{f}_I^{\boldsymbol{\Psi}} = \sum_{\alpha} \int_{\Omega_S^{\alpha} \cup \Omega_H^{\alpha}} \mathbf{B}_I^{\top} \bar{\boldsymbol{\sigma}}_D^{\alpha} \, d\Omega - \sum_{\alpha} \int_{\Omega_S^{\alpha}} \mathbf{B}_I^{\top} \hat{\boldsymbol{\sigma}}_D^{\alpha} \, d\Omega \,, \tag{64}$$

where we have used the fact the $\bar{\boldsymbol{\sigma}}_D^\alpha$ is only non-zero for $\mathbf{x} \in \Omega_S^\alpha \cup \Omega_H^\alpha$ and that $\hat{\boldsymbol{\sigma}}_D^\alpha$ is only non-zero for $\mathbf{x} \in \Omega_S^\alpha$.

To reduce the cost of numerically integrating the singular fields in (56) and (64), the integration of the nodal forces due to the dislocations is transformed as proposed in (10; 38; 39). First, integration by parts is applied to the second term in (64), followed by the application of the divergence theorem, which gives

$$\mathbf{f}_I^{\boldsymbol{\Psi}} = \sum_\alpha \int_{\Omega_S^\alpha \cup \Omega_H^\alpha} \mathbf{B}_I^\top \bar{\boldsymbol{\sigma}}_D^\alpha \, d\Omega - \sum_\alpha \int_{\partial\Omega_S^\alpha} \mathbf{N}_I^\top \hat{\boldsymbol{\sigma}}_D^\alpha \cdot \mathbf{n}_S^\alpha \, d\Gamma + \sum_\alpha \int_{\Omega_S^\alpha \cup \Omega_H^\alpha} \mathbf{N}_I^\top \boldsymbol{\nabla} \cdot \hat{\boldsymbol{\sigma}}_D^\alpha \, d\Omega, \tag{65}$$

where $\partial\Omega_S^\alpha$ is the boundary of Ω_S^α and $\mathbf{n}_S^\alpha$ is the normal to $\partial\Omega_S^\alpha$. Since the enrichments are two-dimensional equilibrium displacement fields, $\boldsymbol{\nabla} \cdot \hat{\boldsymbol{\sigma}}_D^\alpha = 0$ for straight dislocation segments. In this work we neglect the slight violation of $\boldsymbol{\nabla} \cdot \hat{\boldsymbol{\sigma}}_D^\alpha = 0$ for curved dislocation lines. Therefore, the nodal forces due to the dislocations are approximated by

$$\mathbf{f}_I^{\boldsymbol{\Psi}} \approx \sum_\alpha \int_{\Omega_S^\alpha \cup \Omega_H^\alpha} \mathbf{B}_I^\top \bar{\boldsymbol{\sigma}}_D^\alpha \, d\Omega - \sum_\alpha \int_{\partial\Omega_S^\alpha} \mathbf{N}_I^\top \hat{\boldsymbol{\sigma}}_D^\alpha \cdot \mathbf{n}_S^\alpha \, d\Gamma \, . \tag{66}$$

Thus, for the elements containing the singularity, the integral in (56) has been transformed to a surface integral. The computation of the nodal forces due to the dislocation by (66) rather than (56) is critical for the computational efficiency of the model.

The integral in (66) can be written in an equivalent form as an integral over the surfaces of all element boundaries. Though such an approach maybe be simpler to implement, it should be avoided. The evaluation of the integrand in (66) over an element surface through which a dislocation line passes is computationally expensive since the enriched part of the stress $\hat{\boldsymbol{\sigma}}_D^\alpha$ is singular. Furthermore, $\hat{\boldsymbol{\sigma}}_D^\alpha$ is continuous across the faces shared by enriched elements, so the surface integrals over these shared surfaces will cancel each other out. Therefore, only the surfaces on enriched elements which are adjacent to unenriched elements or domain boundary will contribute to (66). The computational efficiency of this surface integral approach is largely due to the fact that the enriched part of the stress $\hat{\boldsymbol{\sigma}}_D^\alpha$ is never evaluated near the dislocation line where it is singular, except in the case where the dislocation line intersects the boundary of the domain.

To further clarify this point, Figure 9a illustrates a dislocation line passing through a cubic domain. The enrichment domain, Ω_S, for the singular enrichment function is chosen so that it completely encloses the dislocation line, as in Figure 9b. Figure 9c illustrates the elements in Ω_S. It is only the outer surfaces of these elements over which the nodal forces due to the dislocation (66) need be computed.

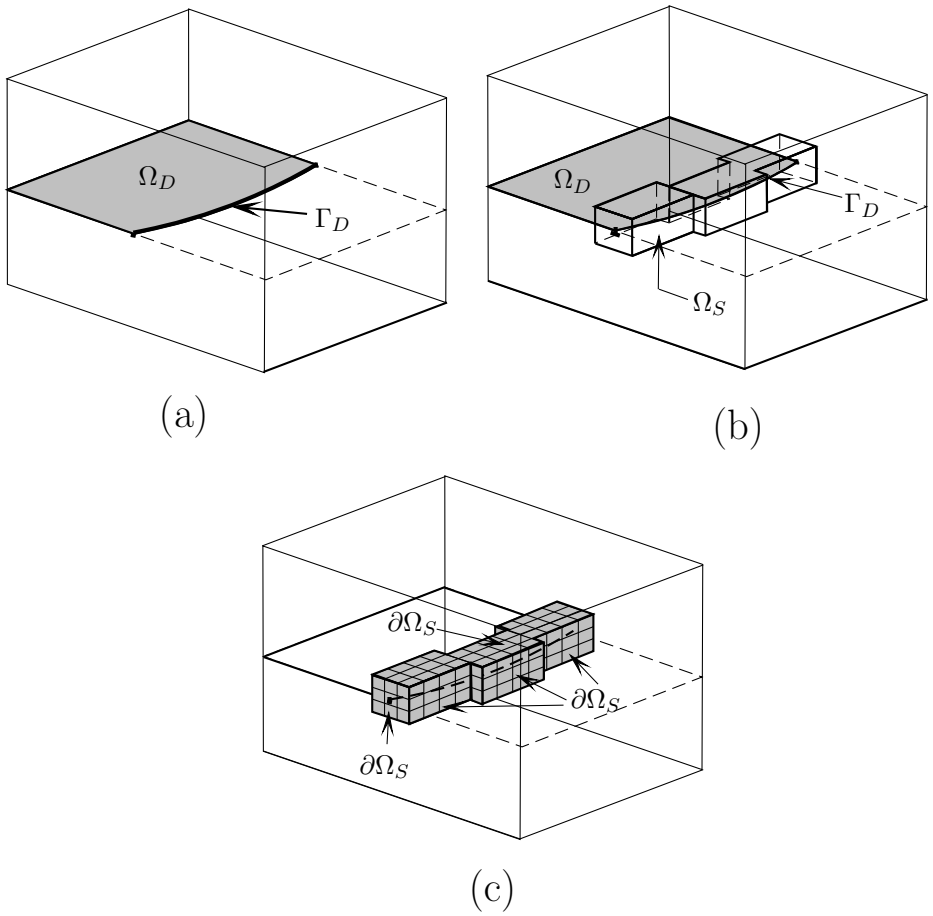

Fig. 9. Illustration of a dislocation line passing through a cubic domain. a) dislocation line Γ_D and slip surface Ω_D. b) Singular enrichment domain Ω_S. c) Elements enriched by the singular enrichment functions.

Finally, we note that the gradient of the enrichment field is a function of the first and second derivatives of the level set fields $f^\alpha(\mathbf{x})$ and $g^\alpha(\mathbf{x})$, see (46). As a result, the gradient of the enrichment is not continuous across element boundaries unless the level set fields are at least C^2 continuous. In this study the level sets $g^\alpha(\mathbf{x})$ and their gradients are represented by C^0 fields (see (41) and (42)) and so the enrichment is also C^0 and does not meet the required continuity; however, our numerical studies suggest that the loss in accuracy is not significant.

3.6 Peach-Koehler force

The configurational forces, i.e. the Peach-Koehler forces, on the dislocation lines are computed as the rate of change in internal energy released from the system with respect to displacement of the dislocation line. In this study, two

methods for computing the dislocation force are compared. The first is the J-integral method derived by Eshelby (40) for linear elastic bodies and by Batra (41) for non-linear elastic bodies. Here we use the equivalent domain form of the J-integral of Moran and Shih (42), which is known to be more accurate than the contour form when applied to fields obtained by finite element approximations. We follow the implementation in (43), where the J-integral is used to compute the stress intensity factors for cracks in three dimensions.

The second method is based on the Peach-Koehler formula (44) and was described in (13) for dislocations modeled with XFEM in two dimensions. The Peach-Koehler force acting at a point $\mathbf{x}^\alpha$ on dislocation Γ_D^α is given by:

$$\mathbf{f}^{PK}\left(\mathbf{x}^\alpha\right) = \boldsymbol{\xi} \times \left(\tilde{\boldsymbol{\sigma}}\left(\mathbf{x}^\alpha\right) \cdot \mathbf{b}\right) \ , \tag{67}$$

where $\boldsymbol{\xi}$ is the local tangent to the dislocation line, $\mathbf{b}$ is Burgers vector and $\tilde{\boldsymbol{\sigma}}\left(\mathbf{x}^\alpha\right)$ is the stress acting on the dislocation line at $\mathbf{x}^\alpha$. This stress is additively decomposed into two parts:

$$\tilde{\boldsymbol{\sigma}}\left(\mathbf{x}^\alpha\right) = \boldsymbol{\sigma}^C\left(\mathbf{x}^\alpha\right) + \tilde{\boldsymbol{\sigma}}_D^\alpha\left(\mathbf{x}^\alpha\right) \ , \tag{68}$$

The first part, $\boldsymbol{\sigma}^C$, is the stress from the standard FEM approximation $\mathbf{u}^C$, i.e. $\boldsymbol{\sigma}^C = \mathbf{C}\boldsymbol{\epsilon}(\mathbf{u}^C)$. It incorporates the stress induced by the applied loads, the finite boundaries (image stress) and by the self stress of the dislocation α. In addition, in contains contributions from far field dislocations. The second part, $\boldsymbol{\sigma}_D^\alpha$ is the contribution of any other dislocation whose core enrichment is nonzero at $\mathbf{x}^\alpha$.

4 Results

4.1 Dislocations in CNTs

To validate the continuum dislocation method for CNTs, we compared the results to atomistic simulations. The atomic simulations were performed using the modified Tersoff-Brenner (MTB-G2) potential (45; 46). MTB-G2 is a modified reactive empirical bond order (REBO) potential (45), where interatomic interactions are included only for atom pairs with a separation of less than 2 Å in the reference configuration (47; 46).

The total energy of the system was minimized at 0 K to obtain the equilibrium geometry. The locations of carbon atoms at the ends of the tube were prescribed to apply the displacement boundary conditions and dangling bonds were terminated with hydrogen atoms. At each strain increment, an energy

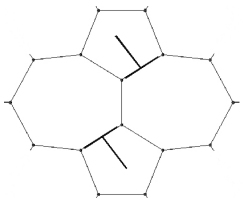

Fig. 10. Stone-Wales defect can be seen as a pair of dislocations, where each 5-7 pair represents a dislocation.

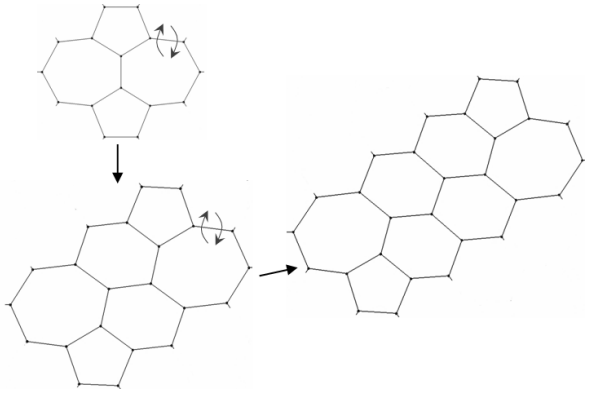

Fig. 11. 5-7 pairs gliding away form each other due to bond reconstructions.

mimimization determined the equilibrium atomic positions by a large scale BFGS quasi-Newton algorithm (48).

4.2 Glide of dislocation by bond rotation

We begin by studying the energetics of a pair of edge dislocations in a CNT under axial loading using both MM and XFEM. In the MM model, the edge dislocation pair is generated by creating a Stone-Wales defect, as shown in Fig. 10. Ding et al. (20) suggested a glide mechanism in CNTs: the side bond of one of the heptagons of the Stone-Wales defect is rotated by 90° and the bonds are reconstructed so that two separated 5-7 defect pairs are generated, as shown in Fig. 11. As this process repeats, the tube diameter shrinks as the length increases.

We consider a [15,15] CNT, 249.6 Å long, containing 6120 atoms. In the MM computations, a Stone-Wales defect was created in the center of the tube and the energy was minimized with carbon atoms along the boundary fixed to obtain an equilibrium geometry. The 5-7 pairs were then allowed to glide away from each other by bond rotation and reconstruction, as shown in Figure 11. The entire glide process was repeated with the CNT stretched by applying appropriate displacements to the carbon atoms at the ends of the tube.

Figure 12(a) shows the dependence of the energy on the separation distance

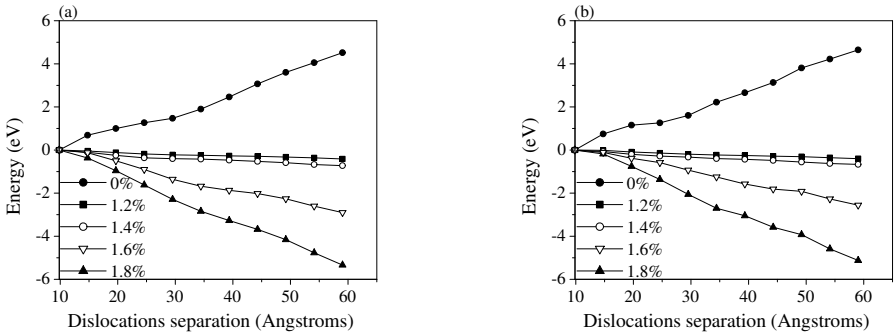

Fig. 12. Energy change at various strains with glide calculated by (a) MM and (b) XFEM for a [15,15] CNT. One glide step corresponds to the Stone-Wales rotation of one bond and $\sim 12^o$ separation between the two dislocation cores.

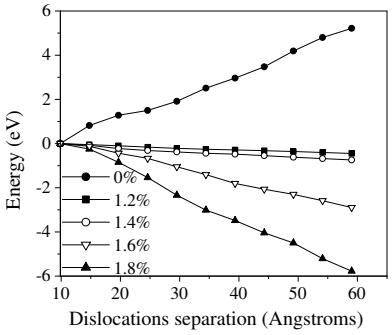

Fig. 13. Energy change at various strains with glide calculated by XFEM using only step function enrichment for a [15,15] CNT.

between two 5-7 pairs at different applied strains. It is observed that when the applied strain is less than 1.2%, the energy of the tube increases as the 5-7 defects move away from each other, suggesting that the gliding process is not energetically favorable. However, as the applied strain becomes more than 1.2%, a decrease in the energy is observed, suggesting that the process of glide becomes energetically favorable when the applied strain is greater than 1.2%. Similar energetics were also observed by Zhang et al. (22) for CNTs in tension and Mori et al. (21) for CNTs under bending. Note that energy is plotted relative to the energy of the tube when the dislocation was 4 glide steps (10 Å) apart at each strain, so the plots show the change in total energy as the dislocation advances. Note that a single glide step separates the dislocation pair by a single hexagon, which is a $\sim 12^\circ$ angular separation for a [15,15] CNT.

We considered the same problem using a continuum shell with a core enriched dislocation model. A cylindrical mesh of the same radius and length as the [15,15] CNT used in the above example was constructed. We used the subdivision surface elements proposed in (34; 35). A finite element mesh of 1440

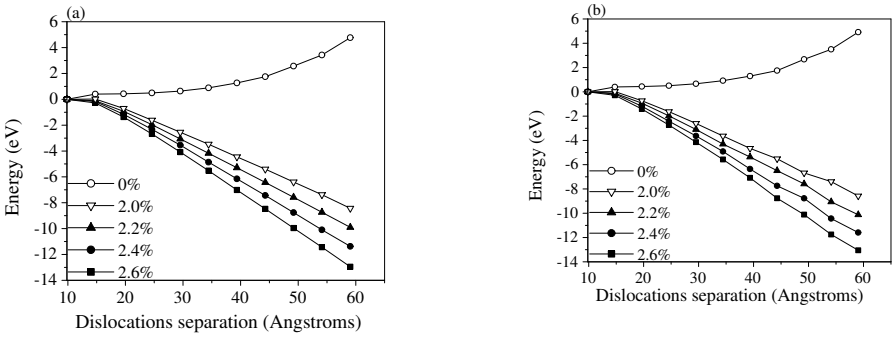

Fig. 14. Energy change at various strains with glide calculated by (a) MM and (b) XFEM for a [50,50] CNT. One glide step corresponds to the Stone-Wales rotation of one bond and $\sim 7.2^o$ separation between the two dislocation cores.

elements of uniform size and 765 nodes was used in the XFEM computations compared to 6120 atoms for the MM calculations. The material properties $E = 730$ GPa and $\nu = 0.4$ were calculated using the MTB-G2 potential and the Burgers vector was $b_\theta = 2.46$ Å. The singular core enrichment was used for nodes within a two Burgers vectors (4.92 Å) from the core. The dislocation cores were moved away from each other along their glide planes to replicate the movement of the 5-7 defect pairs in the MM calculations. Displacement boundary conditions were applied by fixing all degrees of freedom at the ends of the cylinder.

In the continuum model the total energy of the system diverges because $\mathbf{u}^\infty$, (28) is singular. A standard approach to computing the strain energy is to omit a small region around the core in computing the total strain energy. The size of the omitted region was calibrated by matching the energy of the XFEM model with that of the MM model at 0% applied strain and a separation distance of four glide steps between the two dislocation cores. The radius of the omitted region was 2.6 Å, or slightly more than 1 Burgers vector.

Figure 12(b) shows the energy of a dislocation pair calculated by XFEM at different applied strains versus the distance separating the dislocations. Similar to the MM calculations, we observe that after an applied strain of 1.2%, the dislocation motion becomes energetically favorable. The XFEM calculations have the same dependence on applied strain and closely replicate the MM calculations.

We repeated the same set of XFEM calculations using only the tangential step enrichment function (24). Figure 13 shows the energy versus the dislocation separation distance at various applied strains. The results match reasonably well with the MM calculations and with the XFEM computations using the combined singular and tangential step enrichments, (24) and (25), but nearly 8% error was observed in comparison to the singular enrichment XFEM cal-

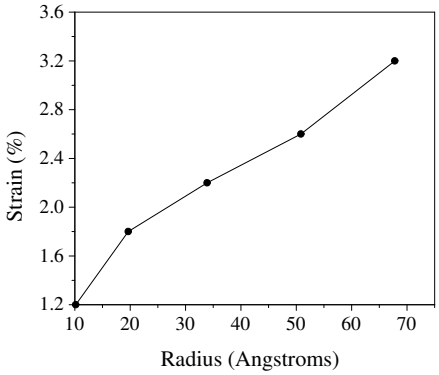

Fig. 15. Tensile strain at which glide becomes energetically favorable with increasing CNT radius.

culations, so the step enrichment is evidently sometimes inadequate for this degree of mesh resolution.

We performed the same set of calculations on a [50,50] CNT of length 249.6 Å using both the MM and XFEM methods to judge the applicability to larger nanotubes where MM becomes expensive. The XFEM model consists of a uniform mesh of 4800 elements and 2550 nodes, in comparison to 20400 atoms in the MM model. The singular core enrichment was used for the nodes within a distance equal to twice the magnitude of the Burgers vector from the cores. The change in energy of the system for different separations between dislocation cores is shown in Figure 14. Similar to the [15,15] CNT, for small applied strain, the energy of the [50,50] tube increases and for high strains the energy decreases as the two dislocations glides away from each other. However, glide becomes energetically favorable at applied strain 2.2%, which is higher than the strain at which the same happens in a [15,15] CNT. In Figure 15, we have plotted these transition strains calculated using XFEM for CNTs with radius as large as 67.8 Å ([100,100] CNT). It is observed that as the tube radius increases the transition strain increases. This is reasonable, since a small CNT has higher initial bending strains, which increase the total strain energy of the tube and cause dislocation glide to become energetically favorable at a smaller applied strain.

4.3 Climb of dislocation by atom removal

We next consider the climb of dislocation pairs due to the removal of atom pairs from the CNT lattice. It was proposed in (20) that the loss of mass observed during CNTs experiments (16) was due to the removal of atom pairs, which leads to the climb motion of a prismatic dislocation. As shown in Figure 16, a two-atom vacancy can be viewed as a dislocation pair. Removal of pairs

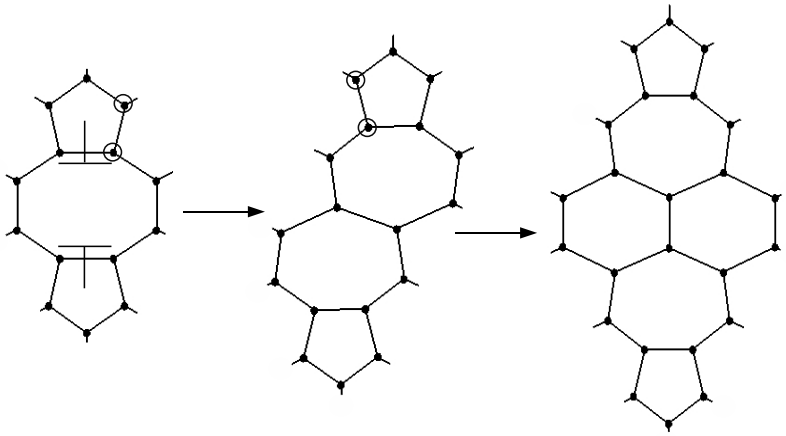

Fig. 16. Climb motion of dislocation due to sequential removal of two-atom pairs (circled atoms).

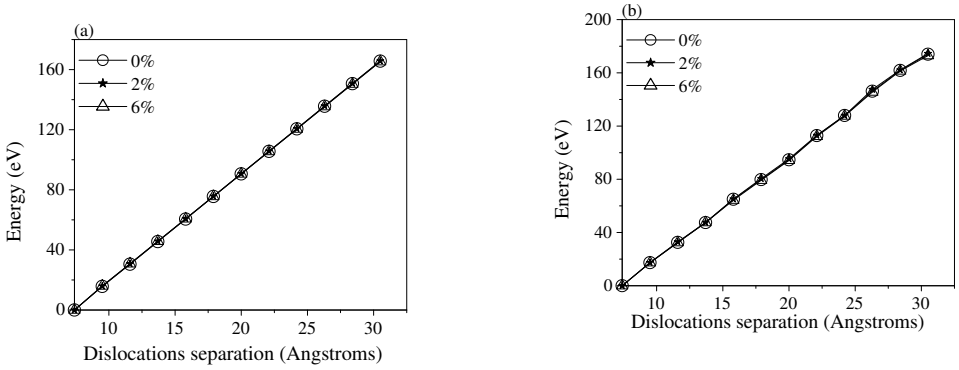

Fig. 17. Energy change at various strains with climb calculated by (a) MM and (b) XFEM for a [10,0] CNT. One climb step corresponds to the removal of two carbon atoms and $\sim$ 2.1 Å separation between the two dislocation cores.

of atoms followed by the reconstruction of bonds induces separation of the dislocation dipole.

We modeled the climb motion first using MM. A two-atom vacancy defect was first created in a 143.5 Å long [10,0] CNT containing 1360 atoms. Pairs of atoms were then removed sequentially so that the climb direction is along the axis of tube. At each step, the energy for the optimized structure was calculated. The same process was repeated after applying tensile strains to the tube. The energy of the tube with respect to the distance between the two cores is shown in Figure 17(a). It increases as the dislocations move away from each other at all applied strains. This suggests that, unlike in the case of dislocation glide, the climb motion is always energetically unfavorable. Note that Figure 17 shows the energies relative to the energy of the tube when both of the dislocation cores have climbed one step away from each other.

The same scenario was modeled by the XFEM dislocation model with a prismatic dislocation pair approximated by (29). The tube geometry was represented by a uniform mesh of 750 elements and 420 nodes. The material properties $E = 915$ GPa and $\nu = 0.4$ were computed from the MTB-G2 potential and Burgers vector is $b_\theta = 2.46$ Å. Note that the Young's modulus of a [10,0] CNT is significantly different from that of a [15,15] CNT. This is one of the idiosyncracies of the MTB-G2 potential (49). While quantum mechanical computations show a constant Young's modulus across all the chiralities of CNTs, the MTB-G2 potential generates anisotropic behavior and hence significantly different Young's moduli in the axial direction for small radii CNTs with different chiralities (49).

As in the glide example, a small region around the dislocation core was omitted in the strain energy calculations. The size of this region was calculated by equating the MM strain energy of the tube after two climb steps (six carbon atoms removed) with the XFEM strain energy of the tube containing a dislocation dipole separated by the same distance. Note that the removal of the first pair of carbon atoms creates a dislocation pair and the removal of next two atom pairs moves the dislocation cores away from each other. The radius of the region omitted about the core was 1.86 Å.

The energies calculated using the XFEM are shown in Fig. 17(b). The results match quite well the MM calculations: the energy increases at all the strains with dislocation climb. Thus, the XFEM model calculations agree closely with the MM models in predicting that the climb motion of dislocation is not energetically favorable. However, at very high temperatures this behavior can be realized due to high thermal energies available to overcome the energy barrier.

4.4 Dislocation loop

In the remainder of this section, we report numerical studies of dislocations in three-dimensional bodies and thin films.

In the first three-dimensional example we compare the accuracy of the stress fields from the XFEM dislocation model with step enrichment versus that with core enrichment. In addition, the Peach-Koehler force computed by the domain form of the J-integral (42) is compared to that computed directly from the XFEM stress field by (67). Consider a dislocation loop of radius $0.25\mu m$ centered in a cubic domain of dimensions $1 \times 1 \times 1\mu$m, as shown in Figure 18. The dislocation loop lies in the plane parallel to the x-y plane. The Burgers vector is parallel to the x-asis and has a magnitude of 5Å. The elastic material properties are $\mu = 62.25$ GPa and $\lambda = 45$ GPa. The domain is subject to a

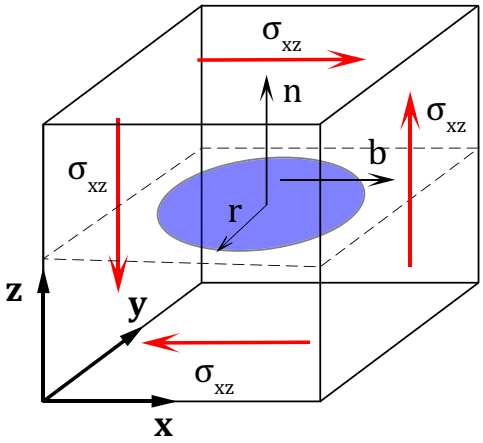

Fig. 18. Illustration of a circular dislocation loop in a cubic domain under a pure shear loading σ_{xz}.

pure shear loading $\sigma_{xz} = 182$ MPa.

Figure 19 compares the stresses σ_{xx} and σ_{xz} along the line passing through the center of the dislocation loop parallel to the x-axis. The stresses are plotted for meshes from $30 \times 30 \times 30$ to $131 \times 131 \times 131$ 8-node brick elements. We see that even with the coarsest mesh, the XFEM solution with core enrichment has nearly converged. On the other hand, the XFEM solution with step enrichment converges slowly. In both cases the computation time is dominated by solving the standard finite element equations, so the core enrichment offers superior accuracy at negligible cost.

Figure 20 compares the Peach-Koehler force computed by the domain form of the J-integral (42) with the solution of the step enriched XFEM and a direction computation of (67) using the solution of the core enriched XFEM (48). The Peach-Koehler forces are shown as vectors radiating from the dislocation line. Results are reported for a fine mesh of $100 \times 100 \times 100$ trilinear elements. The magnitude of the Peach-Koehler force along the dislocation line is nearly constant, as would be expected for a pure shear loading. The results from both methods show good agreement. The maximum difference is about 3%, which we attribute to inaccuracies in the solution obtained with the tangential step enrichment.

4.5 Threading dislocations in layered systems

In this example, we model a layered system with a threading dislocation on a [111] glide plane running along the $[\bar{1}10]$ direction, as shown in Figure 21a. The dimensions of the sample are 2μm$\times 2\mu$m$\times 1\mu m$, where the height of each layer is 500nm. The elastic properties of the system are $\mu_1 = 62.25$, $\mu_2 =$

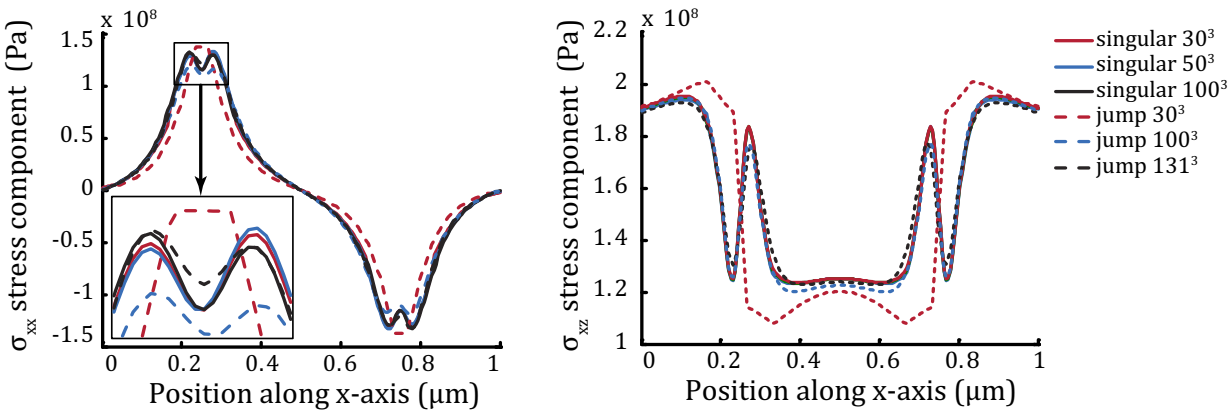

Fig. 19. Comparison of the stresses σ_{xx} and σ_{xz} for the dislocation loop problem computed by XFEM with step enrichment and XFEM with core enrichments for meshes from $30 \times 30 \times 30$ to $131 \times 131 \times 131$ trilinear elements.

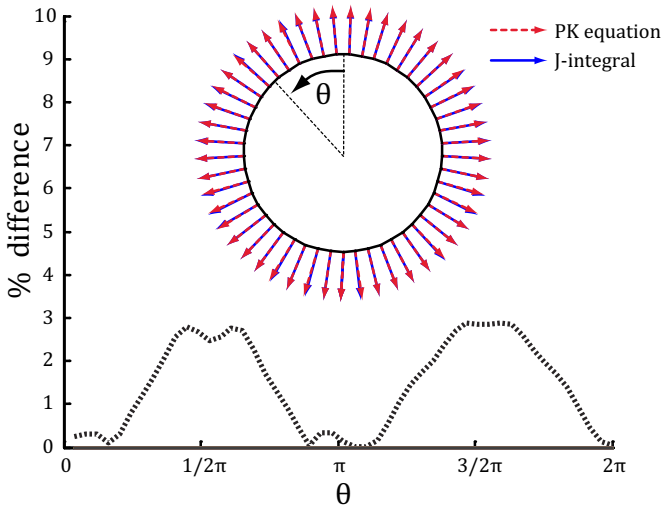

Fig. 20. Comparison of the Peach-Koehler force computed by the domain form of the J-integral (42) and by the Peach-Koehler equation (67).

68.1, $\lambda_1 = 45$, and $\lambda_2 = 52.4$ GPa. The σ_{xx} stress component is plotted in Figure 21b, showing a discontinuity in the stress at the material interface as expected due to the mismatch of material properties. In this problem, the J-integral is problematic because the integration domain is not homogenous when the dislocation approaches the material interface, and therefore singular enrichments are advantageous.

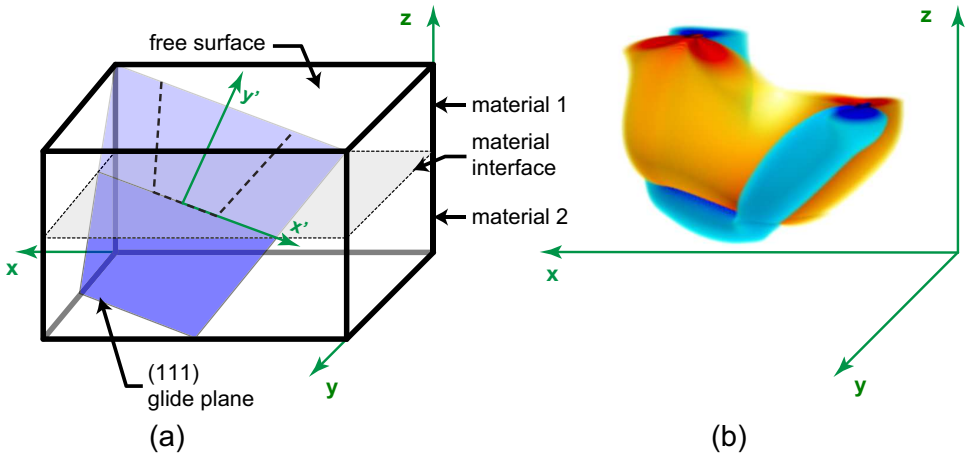

Fig. 21. (a) Epilayer on substrate with a misfit dislocation segment running parallel to the material interface and connected to the free surface by threading segments. (b) σ_{xx} stress contours near the dislocation core computed with a uniform mesh of 100x100x100 elements (3.1 million degrees of freedom).

4.6 Dislocations in misfit layered systems

The singular enrichment is particularly useful when the dislocation is near material boundaries. In the next example, we study a layered system where the lattice mismatch leads to a 1% strain at the material interface. The mismatch is induced by applying a uniform thermal strain in the top material layer. The domain is a unit cube (in microns) with one corner at the origin; the height of each layer is 500nm and the normal direction of the material interface is along the z-direction. The elastic properties of the system are the same as in the previous example. A circular dislocation loop with a 110 nm radius is centered 100 nm above the material interface and 100 nm from the two free surfaces $x = 1$ and $y = 1$, as shown in Figure 4.6. The dislocation loop lies on the [111] plane, and the Burgers vector is in the $[\bar{1}10]$ direction. Boundary conditions are applied on the surfaces $x = 0$, $y = 0$, and $z = 0$ such that the displacement normal to these surfaces is zero. The top surface, $z = 1$, is also a free surface.

The results of the analysis are shown in Figure 23. These forces are due to a combination of the self force on the loop, the interaction with the free surfaces at $x = 1$, $y = 1$, and $z = 1$, the material interface, and the large strain caused by to the mismatch of the materials at the interface. Unlike in superposition methods, the standard finite element field automatically provides the contributions from each of these image fields, without the need to individually compute their contributions. These fields act to shrink the height of the loop, but cause the sides to bow out and travel along the material interface in a

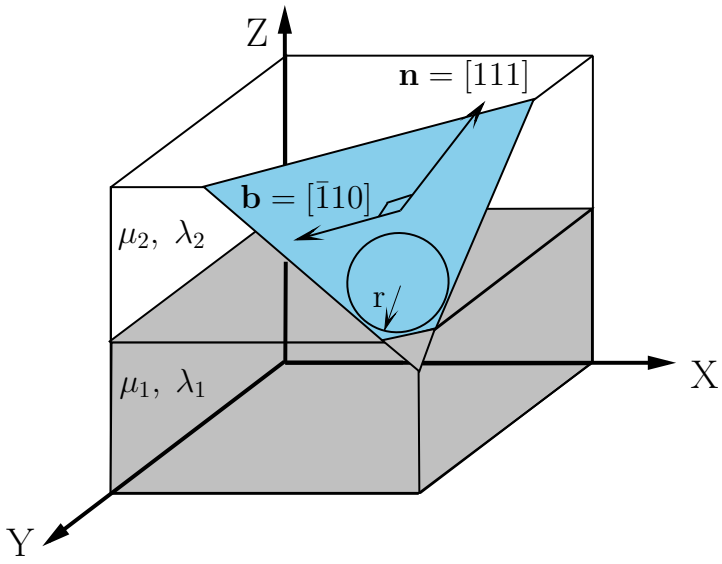

Fig. 22. Illustration of the problem of a dislocation loop in the [111] plane in a thin film.

threading motion.

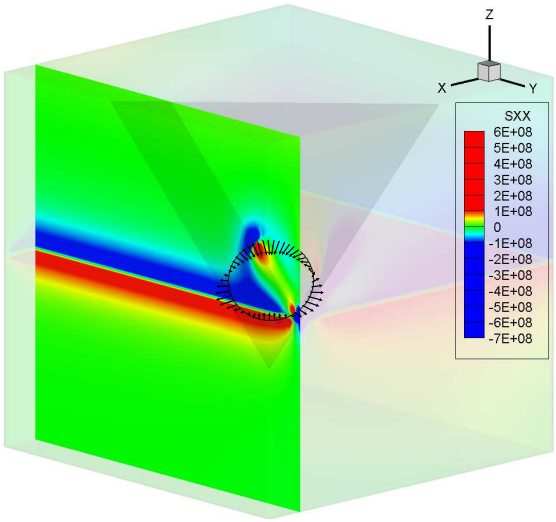

Fig. 23. Peach-Koehler forces computed on a circular dislocation loop in a strained-layered system with misfit strain of 1%. The darkened triangular area shows the [111] glide plane on which the dislocation loop resides, and the contours show the σ_{xx} stresses for a slice at $x = 0.9$.

5 Conclusions

We have demonstrated the capabilities of the Extended Finite Element Method (XFEM) for modeling dislocations in problems involving complex geometry such as carbon nanotubes and three-dimensional thin films. The extended finite element method allows for the addition of local enrichments to the displacement field that model the displacement discontinuity across the glide plane. It also makes possible the addition of singular enrichments around the core by two-dimensional analytical solutions that are transformed to problem-specific local coordinate systems. For thin shells, the near-core singular enrichment is based on a plane stress solution for an edge dislocation in an infinite domain, while in three-dimensions, the near-core singular enrichment are based on plain strain solutions for edge, screw and prismatic dislocations in an infinite domain. In both the shell and three-dimensional models, the effects of the dislocations appear as nodal forces, which arise from integrals over the domains of the elements. In the core-step enrichment scheme, we have employed a transformation, similar to that proposed in (10; 38; 39), which allows the nodal forces to be computed much more efficiently by surface integrals over the boundaries of the singular core enrichment domain.

It was found that the combined core-step enrichment scheme converges much more quickly than the discontinuous step enrichment scheme. Furthermore, the computation of the Peach-Koehler forces in three-dimensional models using core-step enrichments is much less computationally demanding and easier to implement than the evaluation of the J-integrals that are required for models using the discontinuous step enrichment. However, such core enrichments are not available for anisotropic materials, so their applicability is more limited. Step enrichments are applicable to both anisotropic and nonlinear materials.

The thin shell dislocation model was verified by comparison to a Molecular Mechanics (MM) model with a modified Tersoff-Brenner (MTB-G2) potential. The parameters of the continuum model (elastic modulus, Poisson's ratio, and the core cut-off radius) were calibrated by simple MM tests. Simulations of the motion of a pair of edge dislocations in a [15,15] and a [50,50] carbon nanotube by both the continuum and the discrete atomistic models showed that the continuum model predicts very accurate energies. The energies for the XFEM model with the core-step enrichment scheme are nearly indistinguishable from the MM energies; for instance, both models predict that the dislocation motion becomes energetically favorable at 1.2% and 2.2% applied tensile strains for a [15,15] and a [50,50] carbon nanotube, respectively. The energies computed by the XFEM model with the step enrichment scheme are less accurate, but the maximum error is less than 8%. In carbon nanotubes of large radii (up to [100,100]), where MM computation would be very expensive, we have found that the CNTs with larger radii require higher applied strains for the glide

of edge dislocations to become favorable. For example, dislocation motion becomes favorable at 3.3% applied strain in a [100,100] nanotube versus 1.2% strain for a [15,15] nanotube.

We validated the thin shell dislocation model for prismatic dislocations by comparison to MM computations. The energies computed by the XFEM model strongly agree with the MM computations and both methods predict that climb is not energetically favorable at the applied strains studied here.

To the authors' knowledge, the thin shell models presented here is the first continuum model for dislocations in thin shells. Many of the mechanisms of plasticity in carbon nanotubes can now be studied by this computationally more efficient dislocation model.

The modeling of dislocations in three-dimensional bodies by the proposed method with core-step enrichment was validated by comparison to the simpler, yet less efficient, step enrichment. Solutions with these two enrichment schemes were compared for a dislocation loop in a cubic domain under pure shear. In was shown that the stress from the combined core-step enrichment is more accurate and converges more rapidly than that from only the step enrichment - which is similar to what has been found for cracks modeled with XFEM. In addition, it was shown that the Peach-Koehler force computed directly from the stress field of the XFEM solution with both core and step enrichments compares well with that computed by domain integrals with only step enrichment.

We have also studied problems of dislocation loops in thin films. The core-step enrichment was applied to a threading dislocation and to a circular dislocation loop near a material interface with a 1% lattice misfit strain. These examples are difficult for XFEM with step enrichment since the computation of the Peach-Koehler force by domain integrals must be made over a homogeneous domain and illustrate the advantages of the combined core-step enrichment, in which the Peach-Koehler force can be directly computed from the stress. These computations indicate that when a singular near-core enrichment is used, the standard part of the finite element approximation can accurately capture the combined effects of image stresses arising from material interfaces and domain boundaries, dislocation self-stresses, and stresses from other dislocations.

These dislocation models offer substantial promise in the simulation of dislocations in thin films and in thin shells due to their computational efficiency and accuracy and due to the ease by which they can be incorporated into existing FEM software. These are only preliminary developments, but they provide a framework for dislocation dynamics, nonlinear computations, and other challenges.

Acknowledgments

We gratefully acknowledge the grant support from the NASA University Research, Engineering and Technology Institute on Bio Inspired Materials (BIMat) under award No. NCC-1-02037, the support of the Army Research Office under Grant No. W911NF-0510049 and the support of Natural Science and Engineering Research Council under a Canada Graduate Scholarship.

References

[1] N. M. Ghoniem, S.-H. Tong, and L. Z. Sun. Parametric dislocation dynamics: A thermodynamics-based approach to investigations of mesoscopic plastic deformation. *Phys. Rev. B*, 61(2):913–927, 2000.

[2] N. M. Ghoniem and X. Han. Dislocation motion in anisotropic multilayer materials. *Philos. Mag.*, 85(24):2809–2830, 2005.

[3] E. van der Giessen and A. Needleman. Discrete dislocation plasticity: a simple planar model. *Model. Simul. Mater. Sci. Eng.*, 3:689–735, 1995.

[4] K. W. Schwarz. Simulation of dislocations on the mesoscopic scale. i. methods and examples. *J. Appl. Phys.*, 85(1):108–119, 1999.

[5] LP Kubin and G. Canova. The Modelling of Dislocation Patterns. *Scripta Metallurgica et Materialia*, 27(8):957–962, 1992.

[6] JP Hirth, M. Rhee, and H. Zbib. Modeling of deformation by a 3D simulation of multiple, curved dislocations. *Journal of Computer-Aided Materials Design*, 3(1):164–166, 1996.

[7] C. Lemarchand, B. Devincre, and Kubin L.P. Homogenization method for a discrete-continuum simulation of dislocation dynamics. *J. Mech. Phys. Solids*, 49(9):1969–1982, 2001.

[8] S. Groh, B. Devincre, LP Kubin, A. Roos, F. Feyel, and J.L. Chaboche. Dislocations and elastic anisotropy in heteroepitaxial metallic thin films. *Phil. Mag. Lett.*, 83(5):303–313, 2003.

[9] MP ODay and WA Curtin. A Superposition Framework for Discrete Dislocation Plasticity. *JAM*, 71:805, 2005.

[10] G. Ventura, B. Moran, and T. Belytschko. Dislocations by partition of unity. *Int. J. Numer. Meth. Engng.*, 62(11):1463–1487, 2005.

[11] R. Gracie, G. Ventura, and T. Belytschko. A new fast method for dislocations based on interior discontinuities. *Int. J. Numer. Meth. Engng.*, 69:423–441, 2007.

[12] T. Belytschko and R. Gracie. On xfem applications to dislocations in problems with interfaces. *Int. J. Plast.*, 23(10-11):1721–1738, 2007.

[13] R. Gracie, J. Oswald, and T. Belytschko. On a new extended finite element method for dislocations: core enrichments. *J. Mech. Phys. Solids*, 56:200–214, 2008.

[14] J.M. Melenk and I. Babuška. The partition of unity finite element method: Basic theory and applications. *Comput. Meth. Appl. Mech. Eng.*, 139:290–314, 1996.

[15] C.A. Duarte and J.T. Oden. An hp adaptive method using clouds. *Computer Methods in Applied Mechanics and Engineering*, 139(1-4):237–262, 1996.

[16] J. Y. Huang, S. Chen, Z. Q. Wang, K. Kempa, Y. M. Wang, S. H. Jo, G. Chen, M. S. Dresselhaus, and Z. F. Ren. Superplastic carbon nanotubes - conditions have been discovered that allow extensive deformation of rigid single-walled nanotubes. *Nature*, 439(7074):281–281, 2006.

[17] J. Y. Huang, S. Chen, Z. F. Ren, Z. Q. Wang, D. Z. Wang, M. Vaziri,

Z. Suo, G. Chen, and M. S. Dresselhaus. Kink formation and motion in carbon nanotubes at high temperatures. *Phys. Rev. Lett.*, 97(7), 2006.

[18] M. B. Nardelli, B. I. Yakobson, and J. Bernholc. Brittle and ductile behavior in carbon nanotubes. *Phys. Rev. Lett.*, 81(21):4656–4659, 1998b.

[19] A. J. Stone and D. J. Wales. Theoretical studies of icosahedral C60 and some related species. *Chem. Phys. Lett.*, 128(5–6):501–503, 1986.

[20] F. Ding, K. Jiao, M. Q. Wu, and B. I. Yakobson. Pseudoclimb and dislocation dynamics in superplastic nanotubes. *Phys. Rev. Lett.*, 98(7), 2007.

[21] H. Mori, S. Ogata, J. Li, S. Akita, and Y. Nakayama. Energetics of plastic bending of carbon nanotubes. *Phys. Rev. B*, 74(16), 2006.

[22] S. Zhang and T. Zhu. Atomic geometry and energetics of carbon nanotube necking. *Phil. Mag. Lett.*, 87(8):567–574, 2007.

[23] B. I. Yakobson, C. J. Brabec, and J. Bernholc. Nanomechanics of carbon tubes: Instabilities beyond linear response. *Phys. Rev. Lett.*, 76(14):2511–2514, 1996.

[24] C. Q. Ru. Column buckling of multiwalled carbon nanotubes with interlayer radial displacements. *Phys. Rev. B*, 62(24):16962–16967, 2000.

[25] M. Arroyo and T. Belytschko. An atomistic-based finite deformation membrane for single layer crystalline films. *J. Mech. Phys. Solids*, 50(9):1941–1977, 2002.

[26] M. Arroyo and T. Belytschko. Finite element methods for the non-linear mechanics of crystalline sheets and nanotubes. *Int. J. Numer. Meth. Engng.*, 59:419–456, 2004.

[27] S. Zhang, R. Khare, Q. Lu, and T. Belytschko. A bridging domain method for coupled atomistc-continuum modeling of solids. *Int. J. Numer. Meth. Engng.*, 70:913–933, 2007.

[28] Y. Huang, J. Wu, and KC Hwang. Thickness of graphene and single-wall carbon nanotubes. *Phys. Rev. B*, 74(24):245413, 2006.

[29] O. Kraft, LB Freund, R. Phillips, and E. Arzt. Dislocation plasticity in thin metal films. *MRS Bulletin*, 27(1):30–37, 2002.

[30] R.J. Amodeo and N.M. Ghoniem. Dislocation dynamics. i. a proposed methodology for deformation micromechanics. *Phys. Rev. B*, 41:6958–6967, 1990.

[31] K.W. Schwarz. Discrete Dislocation Dynamics Study of Strained-Layer Relaxation. *Phys. Rev. Lett.*, 91(14):145503, 2003.

[32] B. Blanckenhagen, P. Gumbsch, and E. Arzt. Dislocation sources and the flow stress of polycrystalline thin metal films. *Phil. Mag. Lett.*, 83(1):1–8, 2003.

[33] L. Nicola, E. Van der Giessen, and A. Needleman. Size effects in polycrystalline thin films analyzed by discrete dislocation plasticity. *Thin Solid Films*, 479(1-2):329–338, 2005.

[34] F. Cirak, M. Ortiz, and P. Schroder. Subdivision surfaces: a new paradigm for thin-shell finite-element analysis. *Int. J. Numer. Meth. Engng.*, 47(12):2039–2072, 2000.

[35] F. Cirak and M. Ortiz. Fully c-1-conforming subdivision elements for finite deformation thin-shell analysis. *Int. J. Numer. Meth. Engng.*, 51(7):813–833, 2001.

[36] M. Arroyo and T. Belytschko. Finite crystal elasticity of carbon nanotubes based on the exponential Cauchy-Born rule. *Physical Review B*, 69(14):115415, 2004.

[37] N. Moes, A. Gravouil, and T. Belytschko. Non-planar 3D crack growth by the extended Finite element and level setsPart I: Mechanical model. *Int. J. Numer. Meth. Engng.*, 53:2549–2568, 2002.

[38] R. Gracie, H. Wang, and T. Belytschko. Blending in the extended finite element method by discontinuous galerkin and assumed strain methods. *Int. J. Numer. Meth. Engng.*, 0:0–9999, 2008.

[39] G. Ventura, R. Gracie, and T. Belytschko. Fast integration and weight function blending in the extended finite element method. *Int. J. Numer. Meth. Engng.*, 0(0):0–999, submitted.

[40] J.D. Eshelby. The force on an elastic singularity. *Philosophical Transactions of the Royal Society of London. Series A, Mathematical and Physical Sciences*, 244(244):87–112, 1951.

[41] R.C. Batra. The force on a lattic defect in an elastic body. *Journal of Elasticity*, 17(1):3–8, 1987.

[42] B. Moran and C.F. Shih. A general treatment of crack tip contour integrals. *Int. J. Fract.*, 35(4):295–310, 1987.

[43] N. Sukumar, N. Moës, B. Moran, and T Belytschko. Extended finite element method for three-dimensional crack modelling. *Int. J. Numer. Meth. Engng.*, 48:1549–1570, 2000.

[44] M. Peach and J. S. Koehler. The forces exerted on dislocations and the stress fields produced by them. *Phys. Rev.*, 80(3):436–439, 1950.

[45] D. W. Brenner, O. A. Shenderova, J. A. Harrison, S. J. Stuart, B. Ni, and S. B. Sinnott. A second-generation reactive empirical bond order (REBO) potential energy expression for hydrocarbons. *J. Phys.: Condens. Mat.*, 14:783–802, 2002.

[46] T. Belytschko, S. P. Xiao, G. C. Schatz, and R. S. Ruoff. Atomistic simulations of nanotube fracture. *Phys. Rev. B*, 65:235430, 2002.

[47] O. A. Shenderova, D. W. Brenner, A. Omeltchenko, X. Su, and L. H. Yang. Atomistic modeling of the fracture of polycrystalline diamond. *Phys. Rev. B*, 61(6):3877–3888, 2000.

[48] D. C. Liu and J. Nocedal. On the limited memory method for large scale optimization. *Math. Prog. B*, 45(3):503–528, 1989.

[49] S. L. Mielke, D. Troya, S. Zhang, J.-L. Li, S. Xiao, R. Car, R. S. Ruoff, G. C. Schatz, and T. Belytschko. The role of vacancy defects and holes in the fracture of carbon nanotubes. *Chem. Phys. Lett.*, 390(4–6):413–420, 2004.